FOREBODY OPTIMIZATION OF A JET TRAINER AIRCRAFT USING RESPONSE SURFACE METHODOLOGY WITH GENETIC ALGORITHM

A THESIS SUBMITTED TO
THE GRADUATE SCHOOL OF NATURAL AND APPLIED SCIENCES
OF
MIDDLE EAST TECHNICAL UNIVERSITY

BY

ÖMER KANDEMİR

IN PARTIAL FULFILLMENT OF THE REQUIREMENTS
FOR
THE DEGREE OF MASTER OF SCIENCE
IN
AEROSPACE ENGINEERING

SEPTEMBER 2021

Approval of the thesis:

FOREBODY OPTIMIZATION OF A JET TRAINER AIRCRAFT USING RESPONSE SURFACE METHODOLOGY WITH GENETIC ALGORITHM

submitted by **ÖMER KANDEMİR** in partial fulfillment of the requirements for the degree of **Master of Science in Aerospace Engineering, Middle East Technical University** by,

Prof. Dr. Halil Kalıpçılar
Dean, Graduate School of **Natural and Applied Sciences** ________________

Prof. Dr. İsmail Hakkı Tuncer
Head of the Department, **Aerospace Engineering** ________________

Prof. Dr. İsmail Hakkı Tuncer
Supervisor, **Aerospace Engineering, METU** ________________

Examining Committee Members:

Prof. Dr. Sinan Eyi
Aerospace Engineering, METU ________________

Prof. Dr. İsmail Hakkı Tuncer
Aerospace Engineering, METU ________________

Assoc. Prof. Dr. Nilay Sezer Uzol
Aerospace Engineering, METU ________________

Assoc. Prof. Dr. Mustafa Kaya
Aerospace Engineering, Ankara Yıldırım Beyazıt Uni. ________________

Assist. Prof. Dr. Özgür Uğraş Baran
Mechanical Engineering, METU ________________

Date: 01.09.2021

I hereby declare that all information in this document has been obtained and presented in accordance with academic rules and ethical conduct. I also declare that, as required by these rules and conduct, I have fully cited and referenced all material and results that are not original to this work.

Name Last name : Ömer Kandemir

Signature :

ABSTRACT

FOREBODY OPTIMIZATION OF A JET TRAINER AIRCRAFT USING RESPONSE SURFACE METHODOLOGY WITH GENETIC ALGORITHM

Kandemir, Ömer
Master of Science, Aerospace Engineering
Supervisor : Prof. Dr. İsmail Hakkı Tuncer

September 2021, 75 pages

The aerodynamic design of an aircraft's forebody geometry has a significant impact on its performance and stability. Although most studies on aircraft performance have focused on optimizing wing-like structures, the contribution of an effective forebody design to aircraft performance could be as significant as that of wing-like structures. A well-designed forebody can reduce the wave drag and improve the directional characteristics at high angles of attack. The forebody optimization of a jet trainer aircraft in terms of supersonic cruise performance and directional stability is investigated in this thesis. While doing so, two objectives are considered: the wave drag and directional stability. The response surface methodology is used to generate the aerodynamic database, and the non-dominated sorting genetic algorithm–II is used to search for Pareto-optimal solutions. The open-software flow solver SU2 is used to obtain turbulent flow solutions. It is shown that the optimization study enhances the aircraft's performance in terms of wave drag up to 2% and directional stability up to 30%.

Keywords: Aerodynamics, Optimization, Response Surface, Genetic Algorithm, Design

ÖZ

JET EĞİTİM UÇAĞI ÖN GÖVDESİNİN CEVAP YÜZEY YÖNTEMİ VE GENETİK ALGORİTMA İLE ENİYİLENMESİ

Kandemir, Ömer
Yüksek Lisans, Havacılık ve Uzay Mühendisliği
Tez Yöneticisi: Prof. Dr. İsmail Hakkı Tuncer

Eylül 2021, 75 sayfa

Aerodinamik ön gövde tasarımı, hava aracı performansı ve kararlılığı açısından önemli bir etkiye sahiptir. Şu ana kadar hava aracı performansı üzerine yapılan çalışmalar genellikle kanat-benzeri yapıların eniyileştirilmesi üzerine olmasına rağmen, verimli bir ön gövde tasarımının hava aracı performansına katkısı, kanat-benzeri yapıların tasarımından gelen katkı kadar etkili olabilir. İyi tasarlanmış bir ön gövde, dalga sürüklemesini azaltabilir ve yüksek hücum açılarında yanal kararlılığın iyileştirilmesini sağlayabilir. Bu tezde, bir jet eğitim uçağının ön gövde en iyileştirmesi incelenmiştir. Çalışma gerçekleştirilirken, iki adet amaç fonksiyonu dikkate alınmıştır: dalga sürüklemesi ve yönel kararlılık. Türbülanslı akış çözümleri, açık-yazılım akış çözücüsü olan SU2 ile elde edilmiştir. Cevap yüzey yöntemi, aerodinamik veri tabanı oluşturmak için kullanılmış ve Pareto-optimal çözümler ise baskın olmayan sıralama genetik algoritması-II ile elde edilmiştir. Gerçekleştirilen en iyileştirme çalışması, hava aracını dalga sürüklemesi ve yönel kararlılık bakımından iyileştirmektedir. Yapılan eniyileştirme çalışması sonucunda hava aracının performansında dalga sürüklemesi açısından %2'ye, yönel kararlılık açısından %30'a varan iyileştirme gözlemlenmiştir.

Anahtar Kelimeler: Aerodinamik, Eniyileme, Cevap Yüzey, Genetik Algoritma, Tasarım

To my family

ACKNOWLEDGMENTS

I would like to express my greatest gratitude to my supervisor, Prof. Dr. İsmail Hakkı Tuncer, for his continuous support, highly valuable guidance, constructive criticism, and patience. His extensive knowledge in fluid dynamics and optimization have helped me through this challenging time.

It would not be possible to complete my dissertation without the support of my dear parents, Reyhan and Erdal, and my dear sister, Özge. I would like to express my most sincere thanks to my beloved fiancé, Melisa, who always stands by me with her uniqueness.

I would like to thank my dear friends and colleagues, Salih Volkan Özkan and Ali Oğuz Yüksel, for always reminding me to look on the bright side of the problems I have encountered during my research.

I am grateful to Fazıl Selçuk Gömeç for leading me into the optimization field in the first place. I would also like to thank Murat Canıbek and Dr. Erdem Ayan for their support and faith in me.

I would like to thank my colleagues, Berkalp Kamsız, Sergen Sakaoğlu, Onur Küçükoğlu, Bulut Efe Akmenek, Yiğit Fırat Kuşçu, Mehmet Emin Teoman, Kaan Yenipazar and Caner Atlı for providing a joyful work environment.

This thesis is supported by Turkish Aerospace, a subsidiary of Turkish Armed Forces (TSK) and an affiliate of Presidency of Defense Industries (SSB).

TABLE OF CONTENTS

ABSTRACT v

ÖZ vi

ACKNOWLEDGMENTS ix

TABLE OF CONTENTS x

LIST OF TABLES xii

LIST OF FIGURES xiii

LIST OF ABBREVIATIONS xvi

LIST OF SYMBOLS xvii

CHAPTERS

1 INTRODUCTION 1

1.1 Challenges in Supersonic Aircraft Design 2

1.1.1 Effect of Forebody Geometry on Aircraft’s Shock Characteristics 2

1.1.2 Effect of Forebody Geometry on Aircraft’s Directional Characteristics 3

1.2 The Importance of Multi-objective Optimization in Aircraft Design 4

1.3 Objectives and Outline of the Thesis 5

2 METHODOLOGY 7

2.1 Configuration and Design Variables 7

2.2 Response Surface Method 10

2.2.1 Screening Experiments 10

2.2.2 Regression Model 12

2.2.3 Model Accuracy and Performance Assessments 13

2.3 Turbulent RANS Solver: SU2 14

2.3.1 Governing Flow Equations in SU2 14
2.3.2 Reynolds Averaging and Decomposition 17
2.3.3 Turbulence Model.. 17
2.3.4 Spatial Integration.. 18
2.3.5 Time Integration 19
2.3.6 Flux Discretization Scheme 20
2.3.7 Boundary Conditions 21
2.4 Grid Generation 23
3 OPTIMIZATION ALGORITHM 25
3.1 Non-Dominated Sorting Genetic Algorithm - II....................................... 25
4 RESULTS AND DISCUSSION 31
4.1 Grid Convergence Study... 31
4.2 Flow Solutions and Response Surface Formation 35
4.3 Response Surface 39
4.3.1 Screening Experiments 39
4.3.2 Three-level Full Factorial Design 41
4.4 Pareto Optimal Solutions 47
5 CONCLUSION 65
REFERENCES.. 67

APPENDICES

A. Non-dominated Sorting Genetic Algorithm-II Python Code......................... 71

LIST OF TABLES

TABLES

Table 2.1 Grid Generation Considerations 24

Table 3.1: Crowding Distance Algorithm 29

Table 4.1: Flow Conditions used for Objective Function Calculations 39

Table 4.2: Test Dataset Error 45

Table 4.3: Objective Improvements on the Selected Geometries (Predicted / Actual)... 62

LIST OF FIGURES

FIGURES

Figure 2.1: Baseline Configuration 8
Figure 2.2: Lateral Cross-section Design Parameters 9
Figure 2.3: Pressure Far-field Boundary 22
Figure 2.4: Wall Boundaries 22
Figure 2.5: Flow-Chart of Grid Generation 23
Figure 3.1: Uniform Crossover Process 26
Figure 3.2: Mutation Operator 27
Figure 3.3: Genetic Algorithm Process Flowchart 27
Figure 3.4: Graphical Illustration of Crowding Distance Assignment 29
Figure 3.5: NSGA-II Sorting Approach 30
Figure 4.1: Boundary Layer Grid over the Wing 32
Figure 4.2: y^+ Distribution (Re = 82M) 32
Figure 4.3: Surface Grid Densities Used in Grid Convergence Studies 33
Figure 4.4: Variation of Grid Convergence Index 35
Figure 4.5: Continuity and Momentum Residuals 36
Figure 4.6: Streamlines Over the Forebody (0.2 Mach - 25°- AoA - 10° Beta) 37
Figure 4.7: Mach number Distribution @ Y = 0 (1.2 Mach - 1.3°- AoA - 0° Beta) 37
Figure 4.8: Variation of Drag Coefficient 38
Figure 4.9: Variation of Yaw Moment Coefficient 38
Figure 4.10: Standardized Effects for Objective#1 (2^k-Design) 40
Figure 4.11: Standardized Effects for Objective#2 (2^k-Design) 40
Figure 4.12: Variation of $\Delta CD\delta HT$ with $\Delta Cm\delta HT$ 42
Figure 4.13: Standardized Effects for Objective#1(3^k-Design) 43
Figure 4.14: Standardized Effects for Objective#2 (3^k-Design) 43
Figure 4.15: Sample Geometries in the Test Dataset 44
Figure 4.16: Sensitivity Plots for Objective #1 46

Figure 4.17: Sensitivity Plots for Objective #2.. 47
Figure 4.18: Variation of Objective #1 and the Best Drag Configuration 48
Figure 4.19: Variation of Objective #2 and the Best Directional Stability Configuration.. 49
Figure 4.20: Pareto-Optimal Solutions vs Initial Population 50
Figure 4.21: Objectives vs Iteration Count... 51
Figure 4.22: Variation of Design Variables: FR (Top-Left), θ (Top-Right), YC (Bottom-Left) and ZC (Bottom-Right) 52
Figure 4.23: Comparison of NSGA-II results with Weighted Genetic Algorithm . 53
Figure 4.24: Mach number Distribution over the Best Directional Stability Configuration (Top), Lowest Drag Count Configuration (Middle), Moderately Optimal Configuration (Bottom) 54
Figure 4.25: Shock Angles over the Base Configuration (Top-Left), Best Directional Stability Configuration (Top- Right), Lowest Drag Count Configuration (Bottom-Left), Moderately Optimal Configuration (Bottom- Right) 55
Figure 4.26: Pressure Coefficient Distributions over the Base Configuration (Top-Left), Best Directional Stability Configuration (Top- Right), Lowest Drag Count Configuration (Bottom-Left), Moderately Optimal Configuration (Bottom- Right) @ Y=0.. 57
Figure 4.27: Drag Component Percentages for the Base, Best Directional Stability and Moderately Optimal Configurations.. 58
Figure 4.28: Isentropic Mach number Distribution over the Base Configuration (Top-Left), Best Directional Stability Configuration (Top- Right), Lowest Drag Count Configuration (Bottom-Left), Moderately Optimal Configuration (Bottom-Right) 59
Figure 4.29: Streamlines over the Best Directional Stability Configuration (Top), Lowest Drag Count Configuration (Middle), Moderately Optimal Configuration (Bottom) 60

Figure 4.30: Q-criterion Iso-surfaces (TOP-VIEW) @ (0.2 Mach - 25°- AoA - 10° Beta) over the Base Configuration (Top-Left), Best Directional Stability Configuration (Top- Right), Lowest Drag Count Configuration (Bottom-Left), Moderately Optimal Configuration (Bottom- Right) 61
Figure 4.31: Q-criterion Iso-surfaces (SIDE-VIEW) @ (0.2 Mach - 25°- AoA - 10° Beta) over the Base Configuration (Top-Left), Best Directional Stability Configuration (Top- Right), Lowest Drag Count Configuration (Bottom-Left), Moderately Optimal Configuration (Bottom- Right) 62
Figure 4.32: Flow Asymmetry Data for Base and Two-Pareto Optimal Configurations.. 63
Figure 4.33: Q-criterion Iso-surfaces (TOP-VIEW) @ (0.2 Mach - 25°- AoA - 0° Beta) over the Base Configuration (Top), Best Directional Stability Configuration (Middle), Moderately Optimal Configuration (Bottom)....................................... 64

LIST OF ABBREVIATIONS

ABBREVIATIONS

AoA	Angle of Attack
AUSM	Advection Upstream Splitting Method
CFD	Computational Fluid Dynamics
FEM	Finite Element Method
FGMRES	Flexible Generalized Minimum Residual
FVM	Finite Volume Method
FVS	Flux Vector Splitting
GCI	Grid Convergence Index
GMRES	Generalized Minimum Residual
MOEA	Multi-objective Evolutionary Algorithm
NSGA	Non-dominated Sorting Genetic Algorithm
PFF	Pressure Far Field
RANS	Reynolds Averaged Navier-Stokes
RSM	Response Surface Methodology
RSS	Residual Sum of Squares
SST	Shear Stress Transport
SU2	Stanford University Unstructured
TSS	Total Sum of Squares

LIST OF SYMBOLS

SYMBOLS

$\vec{Q}$	Conservative Flow Variable Vector
$\overrightarrow{F_c}$	Convective Flux Vector
$\overrightarrow{F_v}$	Viscous Flux Vector
p	Fluid Static Pressure
T	Fluid Temperature
ρ	Fluid Density
k	Thermal Conductivity Constant
Re	Reynolds Number
Pr	Prandtl Number
C_d	Drag Coefficient
C_m	Pitch Moment Coefficient
C_n	Yaw Moment Coefficient
α	Angle of Attack
β	Side Slip Angle

CHAPTER 1

INTRODUCTION

The idea of supersonic flight was thought to be a myth at the early stages of aviation history. Airplane crashes and incidents while flying near the speed of sound have led to a term called “sound barrier”, a strong belief among many aeronautical engineers that airplanes would never fly faster than the speed of sound. It was a rational argument at that time since the theoretical value of drag rises to infinity as the sonic speed is achieved. Yet, during the presentations of the fifth Volta Conference, the idea of the sound barrier was going to be proven to be the actual myth rather than the supersonic flight itself by the conference attendees in 1935 [1]. Twelve years later, Charles Elwood Yeager would go down in history as the first man to move faster than the speed of sound inside the Bell’s experimental aircraft X-1[2]. Although this was a breakthrough in aviation history, it brought particular concerns regarding aircraft performance and safety issues. With the addition of these supersonic performance and safety concerns to the subsonic flight requirements, the aircraft design became a very challenging process. Within years, many scientists and engineers worked on these concerns and tried to develop solutions to the problems encountered during supersonic flight. The proper design of the external geometry was one of these solutions to diminish supersonic flight performance issues. Although wings represent the most important structure of the external geometry in terms of aerodynamic performance, the forebody geometry also has a significant effect on the aerodynamic characteristics of an aircraft.

1.1 Challenges in Supersonic Aircraft Design

The design of an aircraft is a sequential process that requires multiple disciplines to work incoherence. From the start of the design, important decisions, which will affect the financial success of the design program, have to be taken by each discipline. The earlier these decisions are taken, the higher the impact on the cost of the program [3]. Aerodynamics is one of those disciplines that takes a role in the very early stages of the design process. The decisions taken in the aerodynamic design phase will significantly affect the aircraft's future. To reduce the cost of an aircraft, one shall carefully take the decisions during the aerodynamic design phase.

The aerodynamic design is a critical factor in determining an aircraft's required performance in flight, and it is specifically interested in the aircraft's external structure. These structures consist of wing, canopy, fuselage, forebody, horizontal tail, vertical tail, etc. Wings being the primary structure regarding the main aerodynamic concerns, all of these structures have significant effect on aircraft's performance and stability. Considering the fact that the forebody is the first component encountering the incoming flow, the distortions created on the flow by the forebody will be carried downstream, which will eventually affect the flow distribution over other components of the aircraft. Especially for a supersonic aircraft, the forebody design plays a vital role in aircraft's characteristics.

1.1.1 Effect of Forebody Geometry on Aircraft's Shock Characteristics

In the case of supersonic flight, the flow in the vicinity of an object encounters a phenomenon across which sudden, drastic changes are observed in the flow properties. This phenomenon is called a shockwave, a quite thin region causing losses in the flow. Passing through a shockwave, an increase in the static pressure and a decrease in the total pressure are observed. The sudden increase in the static pressure makes the shockwaves the major source of drag in the supersonic flight and one shall understand the physics of shockwaves to design a feasible supersonic aircraft. The magnitude of the losses and also the increase in the drag force is dependent on the shock strength.

As it is previously mentioned, the forebody is the first component of an aircraft encountering the incoming flow. The shockwaves occurring in the vicinity of the forebody will cause the drag force to increase. Yet, with the right forebody design, the increase in the drag force in supersonic regimes can be effectively reduced by lowering the shock strength.

According to Raymer, the wetted area of an aircraft is the driving factor in friction drag. It can be reduced by using a forebody with a low fineness ratio. A forebody with a low fineness ratio, on the other hand, will result in a high supersonic wave drag [4]. Apart from that, Al-Obaidi and Al-Atabi found out that the nose bluntness also has a high impact on the wave drag at supersonic speeds [5].

1.1.2 Effect of Forebody Geometry on Aircraft's Directional Characteristics

The effectiveness of the forebody is not limited to drag reduction; it also has a significant impact on the directional stability at high angles of attack. Directional stability could be defined as an aircraft's initial tendency to return to its equilibrium point when a side-slip disturbance is given to the aircraft. Poor directional stability constitutes a major risk to the aircraft. Negative directional stability may result in the loss of control over the aircraft.

The effect of the forebody on the lateral and directional characteristics at high angles of attack is investigated by various scientists. At high angles of attack, a forebody with sharp lower corners may initiate a separated vortex, which can have unpredictable effects on the aircraft's intake, wing, and tail surfaces [6]. Chambers found out in 1970 that a proper forebody design may reduce the flow asymmetries at high angles of attack that are present due to increased vortex strength at high angles of attack [8]. On the other hand, the asymmetries present in the flow due to the forebody shape may create a suction force on the forebody and this suction force may provide a favorable contribution to the lateral, directional stability at high angles of attack [7].

1.2 The Importance of Multi-objective Optimization in Aircraft Design

It is possible to meet the requirements specified by the customer or manufacturer with an efficient external geometry design. However, evaluating that efficient design by hand is difficult when there are several requirements that must be met. The design process becomes more difficult, especially when the requirements contradict each other. As a result, an efficient search algorithm must be implemented into the design process in order to find the optimal design that meets all of the requirements.

Unlike single-objective optimization, multi-objective optimization deals with more than one objective function simultaneously. It is possible to see the applications of multi-objective optimization in engineering, economics, and various others. One of the most used multi-objective optimization algorithms is the genetic algorithm which takes the Darwinian evolution theory as the basis. Due to their robustness, genetic algorithms have become increasingly popular for solving optimization problems in aerospace applications [9]. Using a genetic algorithm, Yamamoto optimized an airfoil's lift to drag ratio in a transonic flow and compared the resulting airfoil with a supercritical airfoil [10]. Antunes investigated the effect of the population size of genetic algorithms on the performance of the optimization process of an airfoil [11]. Chen used genetic algorithms to optimize a wind turbine blade for multiple objectives [12]. Genetic algorithms have shown promising results in multi-objective optimization problems in recent studies.

However, the use of sole genetic algorithms may not be a cost-effective way to dive into optimization problems. Especially in aerodynamic design applications where a single point solution is obtained within hours, an optimization using only genetic algorithms may take months to end with today’s computing technology. Therefore, the hybrid usage of genetic algorithms with other surrogate models may be preferable for the optimization studies of aerodynamic configurations. Response Surface Methodology (RSM) is one of these surrogate models which may reduce the computational effort needed in optimization with genetic algorithms. The use of genetic algorithms together with response surface methodology gives feasible and efficient results in optimization studies.

1.3 Objectives and Outline of the Thesis

The studies conducted on the effects of the forebody design exhibit significant changes in an aircraft's aerodynamic performance and stability characteristics. As it is discussed in section 1.1.1, the forebody design plays a vital role in the shock characteristics of an aircraft which significantly affects the cruise performance in a supersonic flight. In addition to that, the high angle of attack stability characteristics of an aircraft is highly dependent on the vortex initiated by the forebody geometry, as explained in section 1.1.2. Therefore, one shall consider these effects in the design of a forebody.

Considering the effects of the forebody design on the aircraft characteristics, two design objectives are selected. The first objective focuses on the minimization of the drag force in the supersonic cruise condition. The minimization of the drag force would result in better fuel efficiency and higher endurance. In order to minimize the drag force, the wave drag caused by the forebody geometry is aimed to be reduced by perturbing the forebody geometry. In the second objective, the directional stability indicator, yawing moment derivative with respect to side-slip angle, at a high angle of attack landing configuration is aimed to be maximized. With the maximization of yawing moment derivative with respect to side-slip angle at a high angle of attack, the aircraft is aimed to gain better departure consistency and improved spin characteristics.

The majority of optimization studies have concentrated on wing-like structures. The goal of this thesis is to demonstrate that a well-designed forebody geometry can be as effective as these structures in terms of aerodynamic performance of the aircraft. To do so, an aerodynamic shape optimization study based on response surface methodology is performed. Design variables are selected based on the design of experiments and computational grids are then generated for perturbed design variables. Then the turbulent flow solutions are obtained for each geometry by using SU2. The design objective values are derived from the flow solutions and used to establish surrogate models using response surface analyses. Finally, the Pareto-optimal solutions are obtained by feeding the resulting response surface models into a non-dominated sorting genetic algorithm-II. As an outcome of this thesis, the supersonic cruise performance and high angle of attack directional characteristics of a jet trainer aircraft are aimed to be improved by an appropriate forebody design.

The process of the forebody optimization is explained in detail in the following chapters. To obtain the design objective values, the aerodynamic flow field around the aircraft must be calculated. The flow field calculation is based on the solution of turbulent RANS equations. The details of RANS equations, the solver used to obtain RANS solutions and the boundary conditions assigned for the solution of RANS equations are discussed in Chapter 2. Apart from that, design variables, the grid generation process and the response surface methodology are also explained in Chapter 2. The non-dominated sorting genetic algorithm-II, which is used to optimize the response surfaces, is discussed in detail in Chapter 3. In Chapter 4, the results of the grid convergence study are first discussed. The accuracy of turbulent flow solutions and the response surface models are then discussed. Following that, the optimal forebody geometries evaluated by the non-dominated sorting genetic algorithm-II are investigated in detail. Finally, the outcomes of this thesis are explained in Chapter 5.

CHAPTER 2

METHODOLOGY

In this section, the methodology used in the optimization study is explained in detail. The forebody geometry is represented by four independent design variables which control the lateral cross-section of the forebody. A grid is then generated for the configurations with the perturbed design variables. Following that, the turbulent flow solutions are obtained at the design points specified in Table 4.1 by using SU2. Aerodynamic coefficients calculated from the turbulent flow solutions are fed into a statistical tool to conduct design of experiments. The idea behind that is to reduce the number of design variables if it is possible. Based on the results of design of experiments, a training data set is generated and the response surface models are obtained for each design objective.

2.1 Configuration and Design Variables

The baseline forebody geometry is provided in Figure 2.1. The baseline configuration has a fineness ratio of 1.9. The midline of the baseline forebody makes an angle of 7.4° with the horizontal axis.

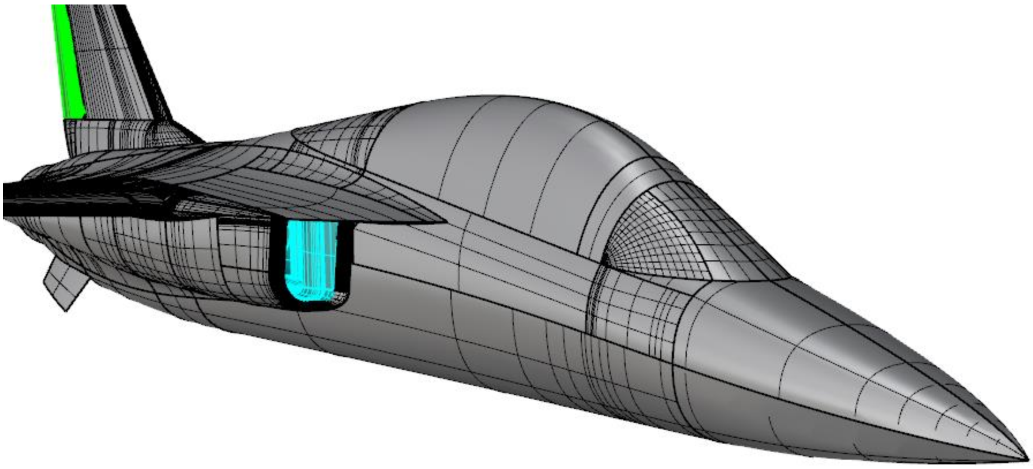

Figure 2.1: Baseline Configuration

In the design of the forebody geometry, four design variables are used to control the lateral cross-section of the forebody geometry [23]. These design variables are listed as follows:

- θ: Nose Deflection Angle
- FR: Fineness Ratio
- YC: Y Spline Coefficient
- ZC: Z Spline Coefficient

Here, nose deflection angle, θ, represents the angle between the horizontal axis and midline of the forebody. Fineness ratio, FR, is the ratio of the length of the forebody to the base cross-section diameter. As the base diameter, the average of the y and z diameters of the base cross-section is used. On the other hand, y and z spline coefficients are used to calculate the radius of the forebody cross-sections at a given x location. The auxiliary-parameters used with the design variables are shown in Figure 2.2. In this figure, L represents the length of forebody geometry. D_y and D_z are diameters at the base cross-section of forebody geometry in y and z directions respectively. x' is the non-dimensional distance in x-direction starting from the forebody apex. It is used for the calculation of the radius in y ($R_{y,x'}$), and in z ($R_{z,x'}$) directions at a given section. The equations used for the calculation of $R_{y,x'}$, $R_{z,x'}$ and FR are given in (2.1), (2.2) and (2.3) respectively.

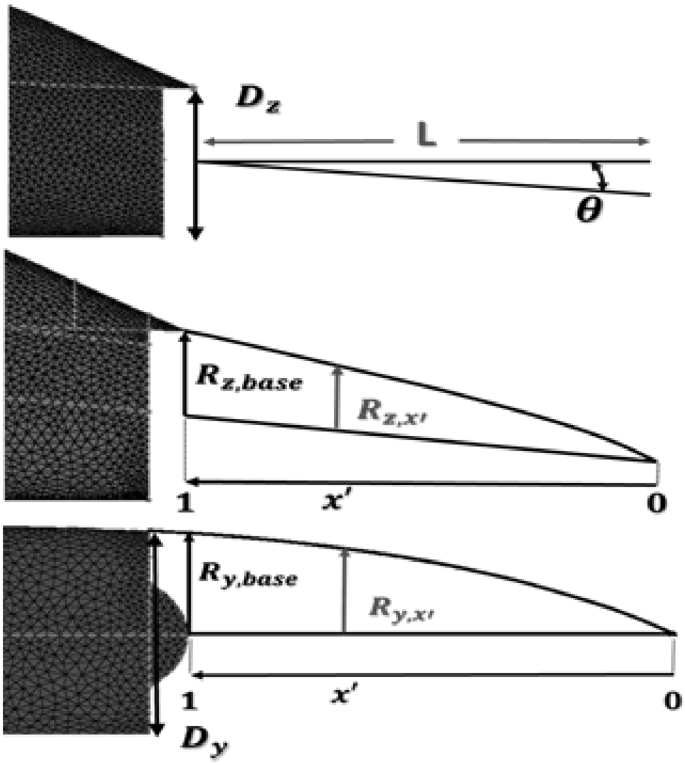

Figure 2.2: Lateral Cross-section Design Parameters

$$R_{y,x'} = \frac{D_y}{2} * \left(1 - x'^{\frac{1}{YC}}\right) \tag{2.1}$$

$$R_{z,x'} = \frac{D_z}{2} * \left(1 - x'^{\frac{1}{ZC}}\right) \tag{2.2}$$

$$FR = \frac{\mathrm{L} * \cos\theta}{\left(\mathrm{D_y} + \mathrm{D_z}\right) * 0.5} \tag{2.3}$$

The reason behind the selection of these design variables is based on the results of experiments conducted previously to observe the effects of the forebody geometry on the design objectives. The fineness ratio is expected to have significant effects on both high angle of attack directional characteristics as Chambers [8] stated and the wave drag according to Raymer [4]. The y and z-spline coefficients control the bluntness of the forebody geometry and are expected to have a significant role in the creation of wave drag , as well, based on the statements of Al-Obaidi and Al-Atabi [5].

2.2 Response Surface Method

Response surface methodology (RSM), which originated in the early 1950s from Box and Wilson’s studies on the effects of environmental factors on a chemical process [26], is a combination of statistical and mathematical techniques to develop, improve and optimize a product or process [27]. In the industrial world, RSM is extensively used in multiple fields ranging from agricultural applications [28] to space studies [29]. Especially, for the cases where several factors influence the performance and quality of a product or process, RSM becomes highly advantageous.

2.2.1 Screening Experiments

RSM applications are performed with a sequential procedure. Before performing response surface analyses, one shall determine the important and unimportant factors on the response by conducting an experiment which is often called a screening experiment. The idea behind the screening experiment is to eliminate the unimportant factors and thereby reduce the number of tests or runs to be conducted for response surface analyses.

To conduct screening experiments, a suitable design shall be selected. The type of the design is dependent on the level of details the experimenter expects to observe. To observe both the main effects and two-way interaction effects, the two-level (2^k) full factorial design becomes the best choice when the number of factors is less than or equal to four [30]. Since there are four design variables (factors) for the case under consideration, 2^k full factorial design is selected to conduct the screening experiments. By taking two points at the minimum and maximum levels of each factor, 16 different configurations are generated in total.

Once the design choice is determined, the responses are obtained by conducting the necessary experiments. By using the response values obtained, the important and unimportant factors are determined. In an experiment, if there are replicates available one can determine the variance of the effects by estimating the variance of the response. Then, the variance of the effects could be used to determine the significant factors on each response. However, for the case under consideration, it is not possible to get replicates since the CFD analyses that provide the response values are based on numerical calculations and will give the same results for each replication. In order to assess the significance of the main and two-way interaction effects when the replicated data is not available, the Lenth's method for estimating the standard deviation of the effects could be used [31]. In this method, a quantity called "Pseudo Standard Error" (PSE) is calculated. Then the significance of the effects is decided based on the margin of error (ME) derived from this quantity. The calculation of ME starts by calculating the absolute value of effect estimate for each factor. So, let c denote the absolute value of the effects. Then it is calculated by the relation shown in (2.4). In this relation, the $\bar{y}_+$ and $\bar{y}_-$ terms correspond to average response values for the observations at the highest and lowest values of each factor respectively.

$$c = \bar{y}_+ - \bar{y}_- \tag{2.4}$$

Following that, 1.5 times the median of effects of each factor is calculated as shown in (2.5).

$$s_0 = 1.5 * median\{|c_i|\} \tag{2.5}$$

Then the PSE is calculated in a similar process by excluding the effects which are greater than the 2.5 times of the s_0 value calculated by using the relation given in (2.5).

$$PSE = 1.5 * median\{|c_i|: |c_i| < 2.5s_0\} \tag{2.6}$$

In the final step, the PSE value computed in (2.6) is multiplied with a factor t obtained from $1 - \alpha/2$ quantile of t-distribution. The term α is the significance level and is taken as 5% for this study. The ME is calculated as follows:

$$ME = t_{1-\alpha/2} * PSE \tag{2.7}$$

The factors with absolute value of effects higher than the ME calculated in (2.7) is assumed to be statistically significant. To display the significant effects, the Pareto chart of standardized effects is used.

2.2.2 Regression Model

The parametric relation between the response and independent variables is established via a regression model. While establishing the relation between the response and predictors, a two-step approach is followed [27]. First a function that estimates the response is found. The general form of this function is shown in (2.8). In this equation, the Y term is the response, the $f(X)$ term is the function used to model the response, the X term represents the predictor matrix including main factors, their interactions and higher order terms of predictors. The β term is the regression coefficient matrix and ϵ is the error term.

$$Y = f(X) + \epsilon, \qquad f(X) = \hat{Y} = \beta X \tag{2.8}$$

Once the model has been selected, the regression coefficients shall be estimated based on the training data set. The regression coefficients shall be selected such that the model error is minimized as much as possible. To find the suitable regression coefficients, the least squares method is used [32]. In the least squares approach, the residual sum of squares (RSS) is minimized. RSS can be expressed as in (2.9).

$$RSS = \sum_{i=1}^{n} \left(Y_i - \widehat{Y_i}\right)^2 \tag{2.9}$$

2.2.3 Model Accuracy and Performance Assessments

To assess the accuracy of the response surface model, the adjusted R-squared is used. Starting from a simple linear model, the adjusted R-squared values are calculated, and the model order is increased until a desired value of an adjusted R-squared is reached. The insignificant interaction and high order terms are removed based on p-statistics provided by MINITAB. The formulation for adjusted R-squared is provided in (2.10). The terms n and p are the number of design points and predictors respectively.

$$R_{adj}^2 = 1 - \frac{RSS(n-p-1)}{TSS(n-1)} \tag{2.10}$$

The RSS term is the residual sum of squares and is provided previously in (2.9). The TSS term, on the other hand, refers to as the total sum of squares and the formulation for that term is provided in (2.11). The $\overline{Y_\iota}$ term is the mean value of the responses and calculated by using the equation described in (2.12).

$$TSS = \sum_{i=1}^{n} (Y_i - \overline{Y_\iota})^2 \tag{2.11}$$

$$\overline{Y_\iota} = \frac{1}{n} \sum_{i=1}^{n} Y_i \tag{2.12}$$

The reason behind using the adjusted R-squared instead of classical R-squared is that the adjusted R-squared uses the number of design points and predictors to assess the model performance. However, the classical R-squared might be misleading in certain conditions where the number of design points is high. The ideal value of adjusted R-squared is 1 which indicates a perfect fit. However, the desired value of adjusted R-squared is generally taken as 0.9 which is set as the cut-off value for the rest of the study.

2.3 Turbulent RANS Solver: SU2

The Stanford University Unstructured (SU2), which has been developed for solving partial differential equation analyses and optimization problems on unstructured grids, is used as the flow solver [14]. The solver has the capability of solving compressible, turbulent flows that are present in fluid dynamics applications. Partial differential equations can be discretized either by using the finite volume method (FVM) or the finite element method (FEM) with an edge-based data structure. Both explicit and implicit schemes are available for time integration and spatial integration could be performed with centered or upwind schemes.

2.3.1 Governing Flow Equations in SU2

Aerodynamic flow field around the aircraft is obtained by solving three dimensional, compressible Navier-Stokes equations. Navier-Stokes equations are the type of non-linear partial differential system of equations derived from conservation of mass, linear momentum and energy equations and could be represented as follows.

$$\frac{\partial \vec{Q}}{\partial t} + \nabla.\overrightarrow{F_c} = \nabla.\overrightarrow{F_v} + \vec{\phi} \tag{2.13}$$

In (2.13), $\vec{Q}$ is the conservative flow variable vector and represented as in (2.14). Where ρ is the density, $\vec{V}$ is the three-dimensional velocity vector which is decomposed into three components (u, v, w) in x, y and z directions in Cartesian coordinates as shown in (2.15). E is the total energy per unit mass.

$$\vec{Q} = \begin{Bmatrix} \rho \\ \rho\vec{V} \\ \rho E \end{Bmatrix} \tag{2.14}$$

$$\vec{V} = \begin{Bmatrix} u \\ v \\ w \end{Bmatrix} \tag{2.15}$$

$\vec{F_c}$ and $\vec{F_v}$ are the convective and viscous flux vectors and represented as in (2.16) and (2.17) respectively. The term p represents the static pressure, whereas k and T represent the thermal conductivity and static temperature respectively.

$$\vec{F_c} = \begin{Bmatrix} \rho\vec{V} \\ \rho\vec{V} \times \vec{V} + p\bar{\bar{I}} \\ \rho E\vec{V} + p\vec{V} \end{Bmatrix} \tag{2.16}$$

$$\vec{F_v} = \begin{Bmatrix} 0 \\ \bar{\bar{\tau}} \\ \bar{\bar{\tau}}.\vec{V} + k\nabla T \end{Bmatrix} \tag{2.17}$$

$\bar{\bar{\tau}}$ is the stress tensor and represented in (2.18) where μ is the dynamic viscosity.

$$\bar{\bar{\tau}} = \begin{bmatrix} \tau_{xx} & \tau_{xy} & \tau_{xz} \\ \tau_{yx} & \tau_{yy} & \tau_{yz} \\ \tau_{zx} & \tau_{zy} & \tau_{z} \end{bmatrix} = \mu \left[\nabla\vec{V} + \nabla\vec{V}^{T} - \frac{2}{3}\bar{\bar{I}}(\nabla.\vec{V}) \right] \tag{2.18}$$

The equation (2.13) could be further expanded in Cartesian coordinates as follows [13]:

$$\frac{\partial \rho}{\partial t} + \frac{\partial \rho u}{\partial x} + \frac{\partial \rho v}{\partial y} + \frac{\partial \rho w}{\partial z} = 0 \tag{2.19}$$

$$\begin{aligned} &\frac{\partial \rho u}{\partial t} + \frac{\partial \rho uu}{\partial x} + \frac{\partial \rho uv}{\partial y} + \frac{\partial \rho uw}{\partial z} \\ &\qquad = -\frac{\partial p}{\partial x} + \frac{1}{Re}\left(\frac{\partial \tau_{xx}}{\partial x} + \frac{\partial \tau_{xy}}{\partial y} + \frac{\partial \tau_{xz}}{\partial z} \right) \end{aligned} \tag{2.20}$$

$$\begin{aligned} &\frac{\partial \rho v}{\partial t} + \frac{\partial \rho vu}{\partial x} + \frac{\partial \rho vv}{\partial y} + \frac{\partial \rho vw}{\partial z} \\ &\qquad = -\frac{\partial p}{\partial y} + \frac{1}{Re}\left(\frac{\partial \tau_{yx}}{\partial x} + \frac{\partial \tau_{yy}}{\partial y} + \frac{\partial \tau_{yz}}{\partial z} \right) \end{aligned} \tag{2.21}$$

$$\frac{\partial \rho w}{\partial t}+\frac{\partial \rho w u}{\partial x}+\frac{\partial \rho w v}{\partial y}+\frac{\partial \rho w w}{\partial z} = -\frac{\partial p}{\partial z}+\frac{1}{Re}\left(\frac{\partial \tau_{zx}}{\partial x}+\frac{\partial \tau_{zy}}{\partial y}+\frac{\partial \tau_{zz}}{\partial z}\right) \tag{2.22}$$

$$\begin{aligned}\frac{\partial E}{\partial t}+\frac{\partial uE}{\partial x}+\frac{\partial vE}{\partial y}+\frac{\partial \rho wE}{\partial z} &= \\ -\frac{\partial up}{\partial x}-\frac{\partial vp}{\partial y}-\frac{\partial wp}{\partial z}-\frac{1}{RePr}\left(\frac{\partial q_x}{\partial x}+\frac{\partial q_y}{\partial y}+\frac{\partial q_z}{\partial z}\right) \\ +\frac{1}{Re}\left(\frac{\partial}{\partial x}\left(u\tau_{xx}+v\tau_{xy}+w\tau_{xz}\right)+\frac{\partial}{\partial y}\left(u\tau_{yx}+v\tau_{yy}+w\tau_{yz}\right)\right. \\ \left.+\frac{\partial}{\partial z}\left(u\tau_{zx}+v\tau_{zy}+w\tau_{zz}\right)\right)\end{aligned} \tag{2.23}$$

In the equations described above, (2.19) is the conservation of mass equation, (2.20), (2.21) and (2.22) are the conservation of linear momentum equations in x, y and z directions respectively and (2.23) is the conservation of energy equation. Re is the Reynolds number and Pr is the Prandtl number. Explicit definitions of Re and Pr are given in (2.23) and (2.24) respectively. In these relations, c is the reference length and c_p is the specific heat coefficient.

$$Re=\frac{\rho V c}{\mu} \tag{2.24}$$

$$Pr=\frac{c_p \mu}{k} \tag{2.25}$$

The Navier-Stokes equations introduced in this chapter consist of six unknowns, yet the number of equations to be solved is five. Hence, one more equation shall be introduced in order to have a closed system. The final equation can be introduced by using ideal gas law as in (2.26). The R term is the universal gas constant.

$$p=\rho R T \tag{2.26}$$

2.3.2 Reynolds Averaging and Decomposition

Osborne Reynolds introduces the Reynolds decomposition of flow variables in the Navier-Stokes equations. Based on that, Navier-Stokes equations are decomposed into mean (time-averaged) and fluctuating components in the following relation shown in (2.27).

$$\emptyset = \overline{\emptyset} + \emptyset' \tag{2.27}$$

The $\overline{\emptyset}$ term is the time averaged value of a random variable whereas the $\emptyset'$ term is the fluctuating components of the random variable. The time averaged values are obtained by integrating the requested variable over time and then dividing the integrated value by the timescale Δt which is large enough compared to fluctuating components. Time averaging relation is given by (2.28).

$$\overline{\emptyset} = \frac{1}{\Delta t} \int_{t}^{t+\Delta t} \emptyset dt \tag{2.28}$$

The Reynolds-Averaged Navier-Stokes (RANS) equations are obtained by substituting the decomposition relation introduced in (2.27) into Navier-Stokes equations.

2.3.3 Turbulence Model

The Reynolds decomposition of Navier-Stokes equations gives rise to an unknown term called Reynolds-stress tensor which has to be modelled in order for the system of equations to be solved. For the case under consideration, Spalart-Allmaras turbulence model is preferred for modelling Reynolds-stress tensor due to its accuracy and robustness [15]. The eddy viscosity is obtained by using Spalart-Allmaras turbulence model as follows:

$$\mu_T = \rho \tilde{v} f_{v1}, \qquad f_{v1} = \frac{x^3}{x^3 + c_{v1}^3}, \qquad x = \frac{\tilde{v}}{v}, \qquad v = \frac{\mu}{\rho} \tag{2.29}$$

The $\tilde{\nu}$ term in (2.29) is the modified kinematic eddy viscosity and the transport equation for this term is given by (2.30).

$$\frac{\partial \tilde{\nu}}{\partial t} + \nabla(\vec{V}\tilde{\nu}) = c_{b1}\tilde{S}\tilde{\nu} + \frac{1}{\sigma}\left[\nabla\big((\nu + \tilde{\nu})\nabla\tilde{\nu}\big) + c_{b2}(\nabla\tilde{\nu})^2\right] - c_{w1}f_w\left[\frac{\tilde{\nu}}{d}\right]^2 \qquad (2.30)$$

The c_{b1}, c_{b2} and c_{w1}terms are the model constants and the d term is the distance to the closest wall. The $\tilde{S}$ term in (2.31) is the production term and calculated by using the relation defined in (2.31).

$$\tilde{S} = |\omega| + \frac{\tilde{\nu}}{\kappa^2 d^2} f_{v2}, \qquad f_{v2} = 1 - \frac{X}{1 + X f_{v1}} \qquad (2.31)$$

The auxiliary parameter f_w used in (2.30) is expressed in detail by (2.32).

$$f_w = g\left[\frac{1 + c_{w3}^6}{g^6 + c_{w3}^6}\right]^{1/6}, \qquad g = r + c_{w2}(r^6 - r), \qquad r = \frac{\tilde{\nu}}{\tilde{S}\kappa^2 d^2} \qquad (2.32)$$

Model constants are given in (2.33).

$$\sigma = \frac{2}{3}, \qquad c_{b1} = 0.1355, \qquad c_{b2} = 0.622, \qquad \kappa = 0.41, \qquad c_{w1} = \frac{c_{b1}}{\kappa^2} + \frac{1 + c_{b2}}{\sigma}, \qquad c_{w2} = 0.3, \qquad c_{w3} = 2, \qquad c_{v1} = 7.1 \qquad (2.33)$$

2.3.4 Spatial Integration

Spatial integration of governing equations over a control volume Ω are performed via finite volume method by applying divergence theorem to (2.13) as follows:

$$\int_{\Omega_i} \frac{\partial \vec{Q}}{\partial t} d\Omega + \sum_{j \epsilon \mathrm{N(i)}} \left(\tilde{F}_{c_{ij}} + \tilde{F}_{v_{ij}}\right) \Delta S_{ij} - \vec{\phi} |\Omega_i| \\ = \int_{\Omega_i} \frac{\partial \vec{Q}}{\partial t} d\Omega + R_i(\vec{Q}) = 0 \tag{2.34}$$

In (2.34), the $\tilde{F}_{c_{ij}}$ and $\tilde{F}_{v_{ij}}$ terms are the numerically approximated versions of convective and viscous flux vectors projected into normal direction respectively. ΔS_{ij} is the area of the face associated with edge ij and $|\Omega_i|$ is the volume of the dual control volume. N(i) represents the neighboring nodes of i$^{\text{th}}$ node. $R_i(\vec{Q})$ is the numerical residual vector. Both types of fluxes are evaluated at the midpoint of each edge and by integrating the evaluated fluxes, the numerical residual vector at each node of the grid is calculated.

2.3.5 Time Integration

Time integration of the integral form of governing equations is performed by using implicit time integration schemes. Implicit integration of time performed on (2.34) leads to the following linear system shown in (2.35).

$$\left(\frac{|\Omega_i|}{\Delta t_i^n}\delta_{ij} + \frac{\partial R_i(Q^n)}{\partial Q_j}\right)\Delta Q_j^n = -R_i(Q^n), \qquad \Delta Q_i^n = Q_j^{n+1} - Q_j^n \tag{2.35}$$

To solve (2.35), a flexible generalized minimum residual (FGMRES) iterative solver is used. FGMRES solver has the capability of handling a wide class of preconditioners in a robust way, however the memory allocation of this solver is twice of the classical generalized minimum residual (GMRES) solver for the same number of iterations [16].

2.3.6 Flux Discretization Scheme

The gradient of the convective flux term in (2.13) forms a hyperbolic system of equations. The discretization of these hyperbolic systems of equations on a grid is adjusted according to the direction in which the information propagates. The idea behind that is based on the fact that the numerical stability of hyperbolic equations is conditional to the identification of upwind direction. In order to identify the upwind directions two different approaches, namely the Godunov (Flux Difference Splitting) approach and the Flux Vector Splitting (FVS) approach are proposed. The FVS approach is simpler and more efficient compared with the Godunov approach and it is a well-suited approach for implicit methods [17]. However, the FVS schemes are not as good as Godunov-type schemes for capturing the discontinuities in the flow.

The flux difference splitting schemes, which are based on the solution of Riemann problem and Godunov's approach, split the difference of the flux vector rather than the flux vector itself as the FVS schemes do. In other words, the flux difference splitting schemes are interested in the waves instead of their direction. By doing so, the oscillations due to discontinuities in the flow are eliminated. Since the exact solution to the Riemann problem requires a highly challenging calculation, certain approximations must be made in order to ease the computational effort. The most popular one among the approximate solvers to the Riemann problem was suggested by Roe in 1981 [18]. Roe approximates the non-linear Riemann problem as a linear problem. For the discretization of convective flux vector, ROE's flux difference splitting scheme is used. The discretization of the viscous flux vector, on the other hand, is done by a scalar upwind scheme.

2.3.7 Boundary Conditions

The system of partial differential equations defined in section 2.3.1 forms a boundary value problem. To obtain the solution to that boundary value problem, a set of boundary conditions must be defined.

2.3.7.1 Farfield Boundary Condition

The pressure far-field (PFF) or often called characteristic boundary condition is used at the outer boundary of the flow field. PFF boundary condition is a commonly preferred boundary condition used in external compressible aerodynamic applications [19], [20] and [21]. It is used to define a free stream condition at a far distance from the object under consideration, such that all the disturbances created on the flow by this object fades out at this boundary. First, the thermodynamic state of the free stream is defined. For the thermodynamic state of the free stream, the SU2 software offers two initialization options. Throughout this study, the default initialization option, in which the free stream density (ρ_∞) is computed by specifying the free stream pressure (p_∞) and temperature (T_∞) at the boundary, is used. After setting the thermodynamic state of the free stream, the flow Mach number and flow direction based on angle of attack (α) and side-slip angle (β), for 3D flows, should be specified. The free stream viscosity (μ_∞) is calculated by using Sutherland's Law [22]. One should note that free stream values that are defined in the far-field boundary are used not only for flow initialization but also for non-dimensionalization.

The PFF boundary is located around 20 times the length of the aircraft away from the position which corresponds to the quarter of the mean aerodynamic chord. A spherical PFF boundary is created in order to provide an almost uniform grid distribution from aircraft body to PFF boundary. The PFF boundary is shown in Figure 2.3.

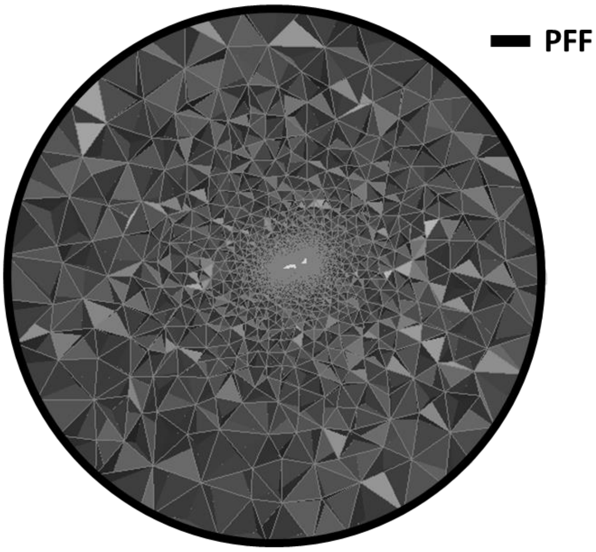

Figure 2.3: Pressure Far-field Boundary

2.3.7.2 Wall Boundary Conditions

The surfaces of the aircraft geometry are attained no-slip wall boundary conditions. Wall boundaries are kept stationary and adiabatic. Adiabatic wall boundary conditions could be expressed such that there is no heat transfer between air and wall boundary. The wall boundaries are shown in Figure 2.4.

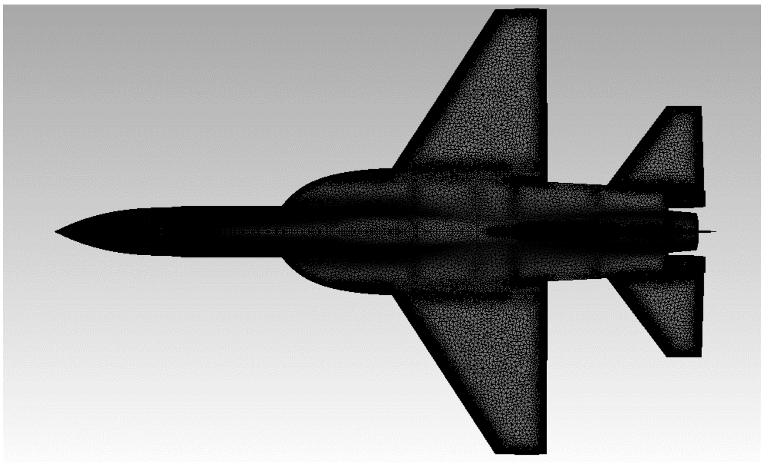

Figure 2.4: Wall Boundaries

2.4 Grid Generation

The grid generation process is completed within three stages. Each of the three stages of the grid generation process is described below. In the first stage, the surface grid is created by using meshing software Pointwise. ANSYS Fluent, on the other hand, is used to generate the volume grid in the second stage of the grid generation. ANSYS Fluent is rather preferred for volume grid generation since it offers more options for prism layer generation, resulting in higher quality grids [24]. In the final section, ICEM-CFD is used in order to convert Fluent ".msh" output into ".cgns" format since the flow solver cannot be used with ".msh" format. A Python code automates the entire process by creating script files for each tool used and then running them in order. The grid generation procedure is summarized in a flow-chart given in Figure 2.5.

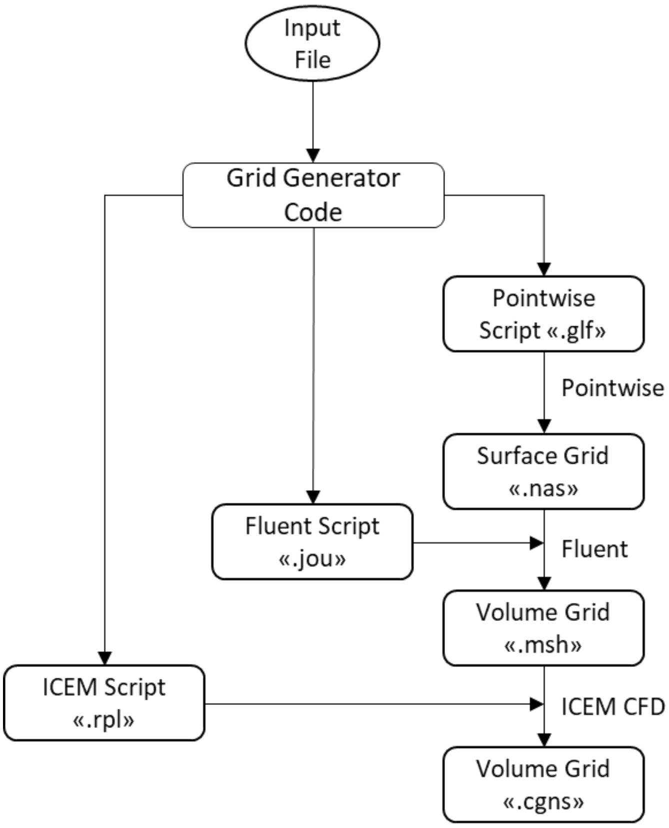

Figure 2.5: Flow-Chart of Grid Generation

A single grid is generated for each geometry such that the first layer height is calculated based on the case with the highest Reynolds number and total boundary layer height is adjusted based on the case with the lowest Reynolds number since it will result in the highest boundary layer height. First layer height and boundary layer height calculations are based on the equations of fully turbulent flow on a flat plate as shown in (2.36) and (2.37) respectively.

$$First\ Layer\ Height = \frac{y^+ * c_{ref}}{Re\sqrt{\frac{C_f}{2}}} \tag{2.36}$$

$$\delta_{BL} = 0.38 * \frac{c_{ref}}{Re^{0.2}} \tag{2.37}$$

Table 2.1 Grid Generation Considerations

Consideration	*Re(10^6)*
$y^+ = 1$	82
$\delta_{BL} \cong 41.7mm$	13.7

CHAPTER 3

OPTIMIZATION ALGORITHM

Aerodynamic coefficients obtained from the SU2 solutions are used as training dataset to be used in data generation with RSM in a statistical analysis tool called MINITAB to generate an aerodynamic database. Screening experiments are conducted by using two-level factorial (2^k) designs to determine the significant factors. Based on the results of screening experiment, a training data set is generated using a three-level factorial (3^k) design, which makes it possible to accurately capture the effects of main and interaction terms. [25]. Following the completion of RSM studies conducted on each objective, the Pareto optimal solutions are obtained using non-dominated sorting genetic algorithm II (NSGA-II).

3.1 Non-Dominated Sorting Genetic Algorithm - II

Non-Dominated Sorting Genetic Algorithm- II (NSGA-II) is a multi-objective search algorithm which is derived from classical evolutionary genetic algorithms. It is based on natural selection and genetics [33]. There stands a simple idea behind this algorithm; “survival of the fittest” which originated from Darwinian evolutionary theory. Based on that theory, the organisms, which adjust themselves to the environment best, survive and inherit their characteristics from generation to generation. In the case under consideration, the organisms are referred to as the geometries produced in the design space and the characteristics are the coded versions of the design variables which are used to generate each geometry.

Before going into the details of NSGA-II, the classical genetic algorithm is going to be explained first since it is easier to follow. The genetic algorithms are a sequential process in which three stages are followed. The first stage is the reproduction stage in which the fittest individuals from a population are selected to reproduce offsprings which inherit the characteristics of their parents. This stage is nothing but the artificial version of natural selection in genetics. In the second stage, an operator called crossover takes place. This operator is used to exchange the critical information via genes between the selected individuals (parents). By this process several off-springs are produced based on crossover probability. One of the most used crossover methods, uniform crossover, is shown in Figure 3.1. In this type of crossover, a crossing site selected in the chromosomes of each parent and genes at the opposite sites of the crossing site are exchanged between the parents to form offspring.

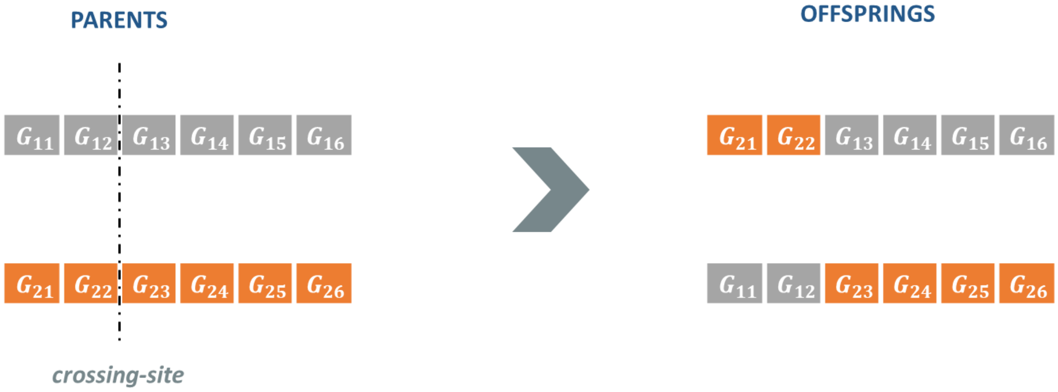

Figure 3.1: Uniform Crossover Process

In the final stage of the genetic algorithm, the mutation operator takes place. The mutation operator changes the genes in a chromosome to maintain the diversity within the population. The genes in a chromosome are subjected to mutation operation with a low, random, and equal probability. Because of the low probability of occurrence, the mutation operation has a secondary effect in the application of genetic algorithms. Although mutation operator has a secondary effect, it plays a vital role to avoid being stuck in a local minimum [33].

Figure 3.2: Mutation Operator

Once all three operators are applied to a population of an ith generation, parent and offspring populations go under a sorting operation. Following that, the first portion of the sorted population with the same size of the initial population is selected to reproduce the offspring population in the next generation. The remaining portion is rejected automatically. This process is repeated until a convergence criterion is achieved. The criterion could be either the maximum number of generations or a custom user defined function. The summary of the process is given in Figure 3.3.

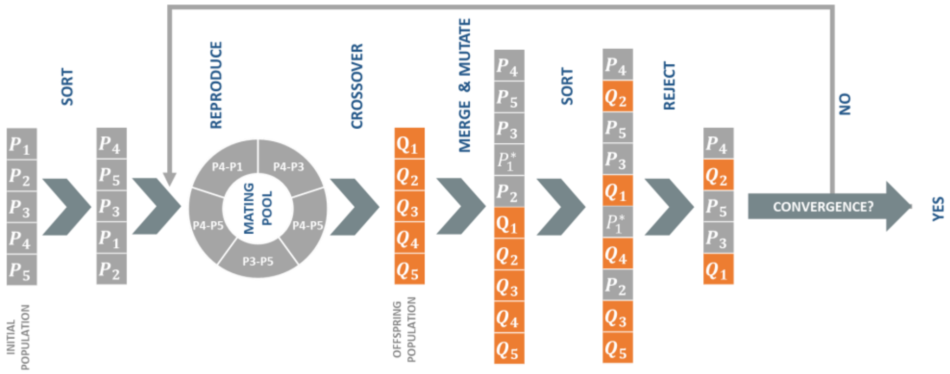

Figure 3.3: Genetic Algorithm Process Flowchart

The basics of classical genetic algorithm structure is summarized above. Besides that, all the operators summarized are based on a single objective problem. However, most of the cases faced in engineering problems have more than one objective. In the presence of several objectives, a set of optimal solutions (also known as Pareto-optimal solutions) are obtained rather than a single solution. NSGA-II is a type of multi-objective evolutionary algorithm (MOEA) that is developed to reduce the computational complexity of such evolutionary algorithms that uses non-dominated sorting [34]. Like classical single objective genetic algorithms, NSGA-II also involves reproduction, crossover and mutation operators with slight modifications applied to sorting algorithms.

In NSGA-II, the sorting algorithm is divided into two as non-dominated sorting and crowding distance sorting. In non-dominated sorting approach, an individual p is said to dominate another individual q if and only if the following conditions are true [35]:

I. Individual p has no objective worse than that of individual q.
II. At least one objective of individual p is better than that of individual q.

In the non-dominated sorting approach, each individual is assigned two entities: the domination count n_p which is nothing but the number of individuals that dominates individual p and a set of solutions S_p that is dominated by individual p. The individuals with a domination count of zero will be placed in the first non-dominated front. Then for each individual p in the first non-dominated front, the domination count of each individual q of set S_p is reduced by one. The individuals with a non-domination count of zero, if there are any, are put into a separate list Q which is the second non-dominated front. This procedure is repeated until all the fronts are identified in the population.

In the second part of the sorting algorithm of NSGA-II, the crowding distance sorting approach is assigned. Crowding distance is used to sort the individuals belonging to the same front. This entity could be represented as the absolute difference in the normalized objective values of two adjacent individuals belonging to the same non-dominated front. The crowding distance assignment to each individual in the same front is performed by using the algorithm shown in Table 3.1. In a non-dominated set S, the crowding distance entity (d) for each individual is set to zero. Following that, the individuals are sorted in an ascending order for each objective m and the crowding distance values of the individuals at the boundary points are set to infinity. Hence, the individuals with smallest and largest objective values in a non-dominated set are always selected. For the remaining each individual i, the crowding distance assignments are performed by using the nearest neighbor's objective function values.

In Table 3.1, the term f_m^i stands for the m^{th} objective function value of i^{th} individual. The terms f_m^{max} and f_m^{min} stand for the maximum and minimum values of m^{th} objective function in a non-dominated set S respectively. A visual is provided in Figure 3.4 to clarify the logic behind crowding distance assignment.

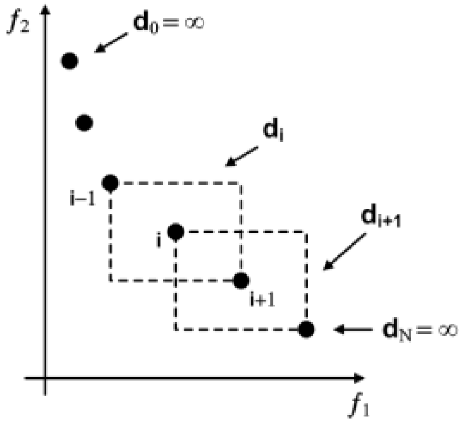

Figure 3.4: Graphical Illustration of Crowding Distance Assignment

Table 3.1: Crowding Distance Algorithm

```
$l = size(S)$
$for\ each\ i\ in\ S$
    $dist(i) = 0$
$for\ each\ objective\ m$
    $S = sort(S,m)$
    $d(1) = d(l) = \infty$
    $for\ i = 2\ to\ l-1$
        $d(i) = d(i) + (f_m^{i+1} - f_m^{i-1})/(f_m^{max} - f_m^{min})$
```

The crowding distance sorting is useful in the cases where a certain part of a non-dominated front cannot be passed to the next generation and must be eliminated. The crowding distance entity preserves the diversity in a population [34]. Both the non-dominated sorting and crowding distance approaches are provided in a scheme in Figure 3.5.

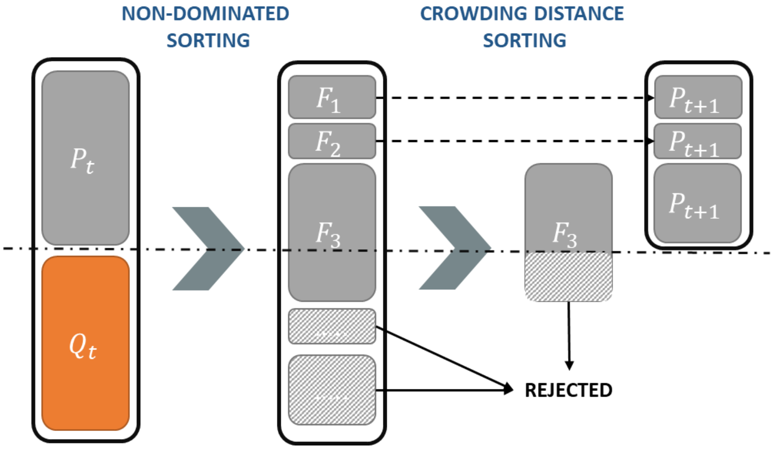

Figure 3.5: NSGA-II Sorting Approach

CHAPTER 4

RESULTS AND DISCUSSION

Based on the methodologies explained in Chapter 2 and Chapter 3, the results are obtained and discussed within this chapter. First, a grid convergence study is conducted. Grid independent flow solutions obtained by using SU2 are discussed in terms of accuracy. Then, the response surface models are validated. Finally, the Pareto-optimal design configurations obtained by NSGA-II are analyzed at the flow conditions provided for design objectives and the results are compared to RSM predictions.

4.1 Grid Convergence Study

The grid generation criterions for this study have been previously defined in Table 2.1. In the first criterion it is stated that boundary layer height shall be approximately 42 mm. To capture the boundary layer properties accurately, the initial grid generated from the wall boundaries is formed by a special type of cells called prism cells in ANSYS Fluent. To see whether the first grid generation criterion is satisfied or not, one can observe the slice taken over the volume grid at the quarter span of wing geometry shown in Figure 4.1. 43.8 mm of total prism layer height is achieved as it can be seen in Figure 4.1. Since the total prism layer height is over the value of boundary layer height specified in Table 2.1, it can be stated that the first criterion for grid generation is satisfied.

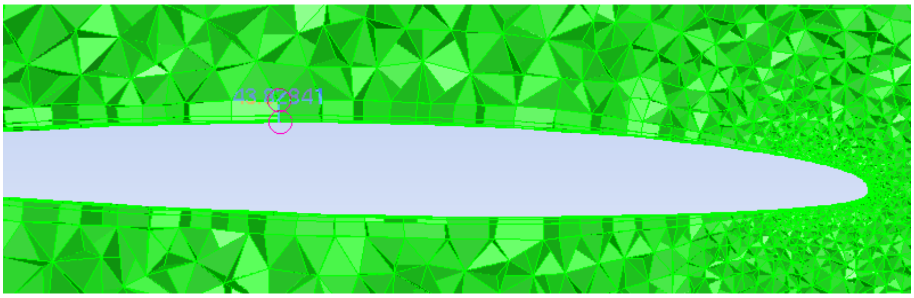

Figure 4.1: Boundary Layer Grid over the Wing

Another criterion, that has been specified for grid generation in Table 2.1 in the previous chapter, was the y^+ value. The y^+ value is important for capturing turbulent properties so that the effect of viscous forces on aerodynamic coefficients is obtained as accurately as possible. The Spalart-Allmaras turbulence model in SU2 requires resolving the fully turbulent viscous sublayer. Therefore, the y^+ value shall be less than 1 as it is given in Table 2.1. In Figure 4.2, the y^+ value distribution over the aircraft surfaces for the case with 82M of Reynolds number is given as a contour plot. Overall, the value is below one. Yet, at certain parts of the aircraft, especially at the leading edges where separation bubbles are observed, the maximum value of y^+ reaches up to 1.6. However, one shall note that the parts of the aircraft with y^+ value above 1 cover only a small portion of the aircraft's external surface.

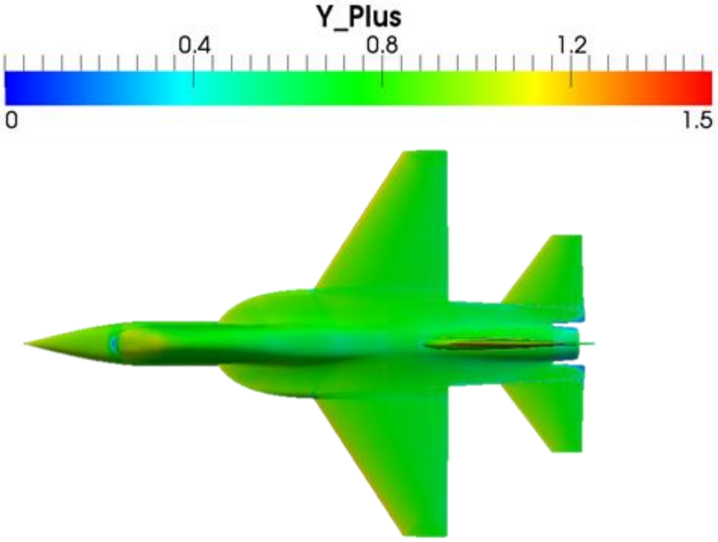

Figure 4.2: y^+ Distribution ($Re = 82M$)

The grid generation criterions discussed above is mainly satisfied. Hence, the studies conducted on the grid convergence could be further discussed. While conducting grid converging studies, five different grids with five different node element counts ranging from 3M to 20.4M are used. In Figure 4.3, three of the grids with the node element counts (in the volume grid) of 3.2 M being the coarsest, 7.2M being the medium and 20.2M being the finest grid are displayed. Starting from the coarsest grid, the surface grid nodes are doubled in size and the maximum edge length is halved. The volume grid generation, on the other hand, is done by considering the constraints specified in Table 2.1 for each grid separately.

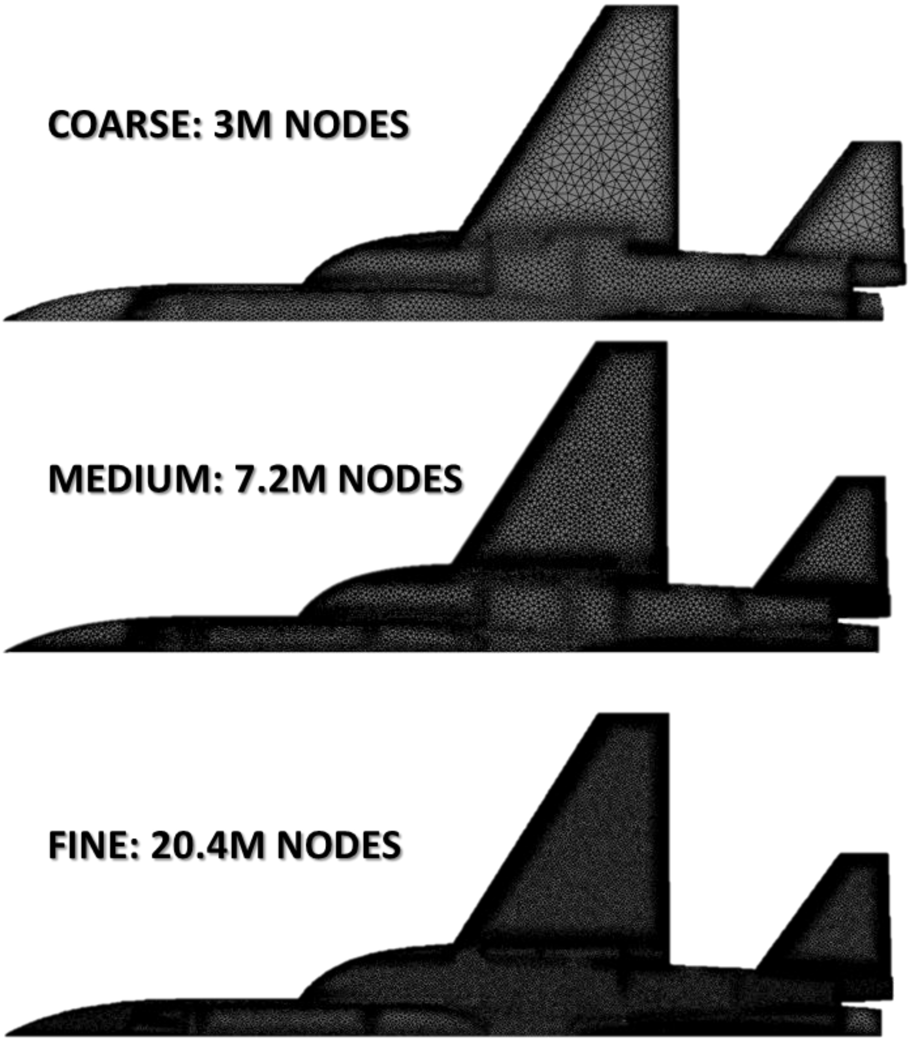

Figure 4.3: Surface Grid Densities Used in Grid Convergence Studies

There are several ways to decide on selecting the grid to continue with. In this study, Roache's grid convergence index (GCI) derived from Richardson extrapolation [36] is used as the grid convergence criteria since it compares the changes in the objective function with respect to grid sizes regardless of the objective function's order of magnitude. Roache's GCI is calculated by using the formulation expressed in (4.1). In equation (4.1), the term r refers to the grid refinement ratio which is nothing but the ratio of the fine grid's node count to that of coarse grid. On the other hand, the terms p and F_s are the order of magnitude which is taken as 2 and the safety factor which is set to 3 by default respectively. The ϵ term corresponds to the percent change in the objective function value from fine to coarse grid. It is expressed in more detail by the equation shown in (4.2). In this equation, the terms $\emptyset_1$ and $\emptyset_2$ correspond to the objective function values of fine and coarse grids respectively.

$$GCI_{fine\,grid} = \frac{F_s\,|\epsilon|}{r^p - 1} \tag{4.1}$$

$$\epsilon = \frac{\emptyset_1 - \emptyset_2}{\emptyset_1} \tag{4.2}$$

By using the relations shown in (4.1) and (4.2), the grid convergence index for the four out of five grids excluding the most coarse one (since the relation given in (4.1) is used for only the fine grid) is calculated and the results provided in a graph in Figure 4.4. It is possible to observe from Figure 4.4 that the Roache's GCI for yawing moment coefficient decreases significantly after the first grid size and then no significant change is observed. On the other hand, the Roache's GCI calculated for drag coefficient is already at a significantly low value. Hence, the grid with 7.2M node elements is used for the rest of the study.

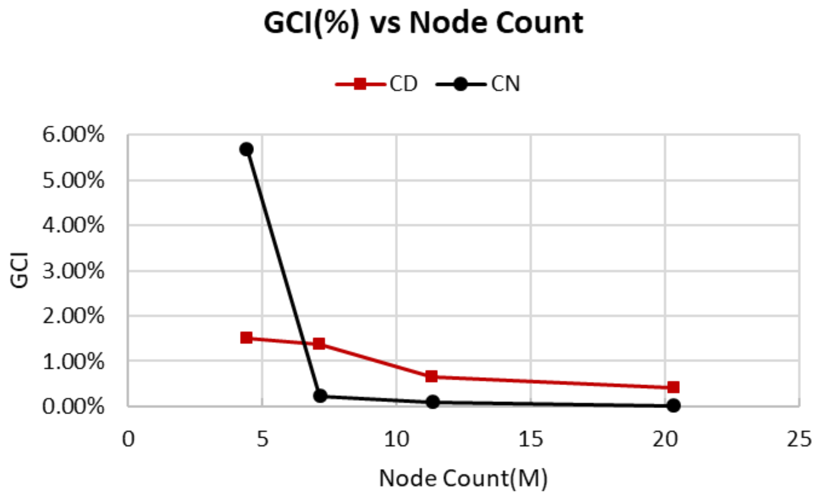

Figure 4.4: Variation of Grid Convergence Index

4.2 Flow Solutions and Response Surface Formation

In section 2.3, it is mentioned that SU2 is used in order to obtain the turbulent flow solutions around aircraft. In this section, the results obtained by SU2 are going to be investigated by using the open-software post-process tool ParaView. First the convergence of the flow solutions is investigated by checking the continuity and momentum residuals. In Figure 4.5, the logarithm of the root mean square (RMS) of the density and x-momentum residuals are provided for the supersonic cruise condition and high angle of attack case. The maximum number of iterations is selected as 3000, 500 iterations of first order and 2500 iterations of second order solutions. The total wall-clock time for full iteration solutions by using 480 cores is around 55 minutes. Based on the residual plots, both the continuity and x-momentum residuals drop to 10^{-8} for the supersonic cruise condition. For the high angle of attack case the residuals are slightly higher. The jumps in the residual histories correspond to the iteration where the solution order is switched to the second order.

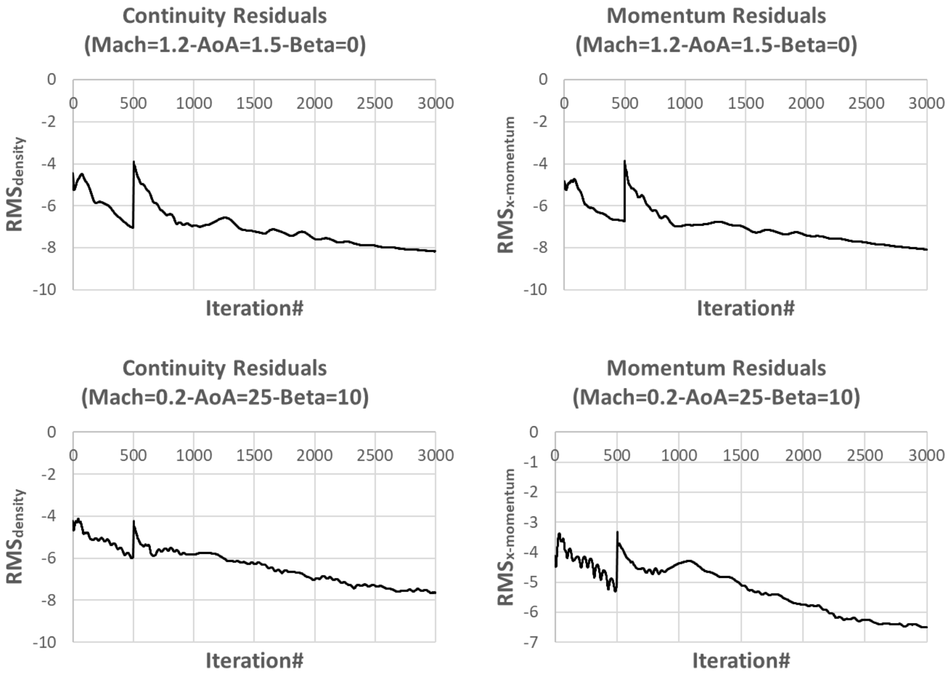

Figure 4.5: Continuity and Momentum Residuals

Following the convergence check, an investigation is conducted by tracing the streamlines passing through the apex of the forebody. In Figure 4.6, the streamlines passing through the apex of the forebody for the flow solution with 0.2 Mach number, 25° of angle of attack and 10° of side-slip angle are provided. One can observe that the streamlines are directed towards the vertical tail which will eventually disturb the pressure distribution over the vertical tail. Wider the forebody gets in the y-z plane, the higher the possibility that the vertical tail is in the wake of the forebody. Therefore, the directional stability is expected to be affected significantly with the shape of the forebody based on not only the statements of Chamber’s experiments conducted in Langley Research Center [8] but also the SU2 results.

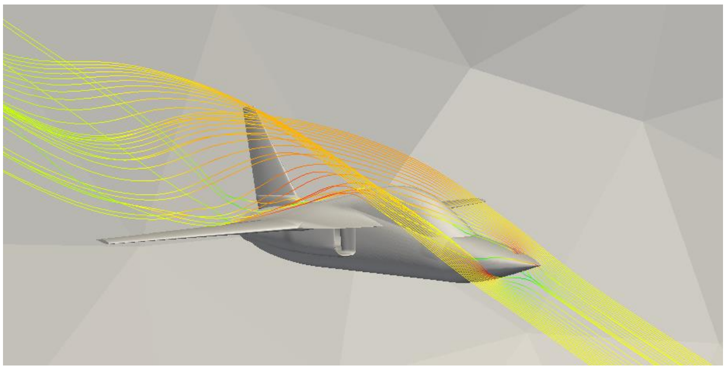

Figure 4.6: Streamlines Over the Forebody (0.2 Mach - 25°- AoA - 10° Beta)

Another investigation is conducted by observing the Mach distribution at a slice taken at y = 0. In Figure 4.7, the Mach number distribution at a slice taken at y = 0 is shown for the flow solution with 1.2 Mach number, 1.3° of angle of attack and 0°of side slip angle. The supersonic incoming flow encounters a flow phenomenon passing through the forebody apex and the flow speed is decreased to a level below sonic speed which is an indicator of a strong shock formation. The strength of the shock is highly dependent on the deflection angle of the obstacle from the incoming flow direction. Higher the deflection angle, the stronger the shock becomes. It is expected to observe a reduction in the shock strength forming at the apex of the forebody by designing a high fineness ratio forebody with a low z-spline coefficient which will result in a lower deflection angle from the incoming flow direction.

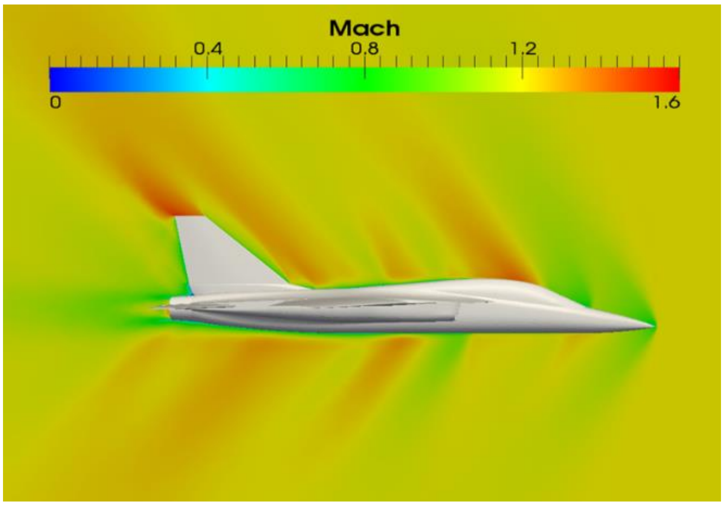

Figure 4.7: Mach number Distribution @ Y = 0 (1.2 Mach - 1.3°- AoA - 0° Beta)

SU2 is a validated flow solver. Figure 4.8 shows the variation of drag coefficient at 0° of angle of attack with respect to Mach number ranging from 0.2 to 1.3 for both SU2 and wind tunnel test results. As observed, the drag coefficients predicted are in general in good agreement with experimental data in all Mach regimes. In Figure 4.9, the variation of yaw moment coefficient at 0.3 Mach and 25° of angle of attack with respect to side slip angle ranging from 0° to 10° is similarly shown for both SU2 and wind tunnel test data. Although the deviations are higher compared to the ones observed in drag coefficient comparison, the trend in the data seems to be captured.

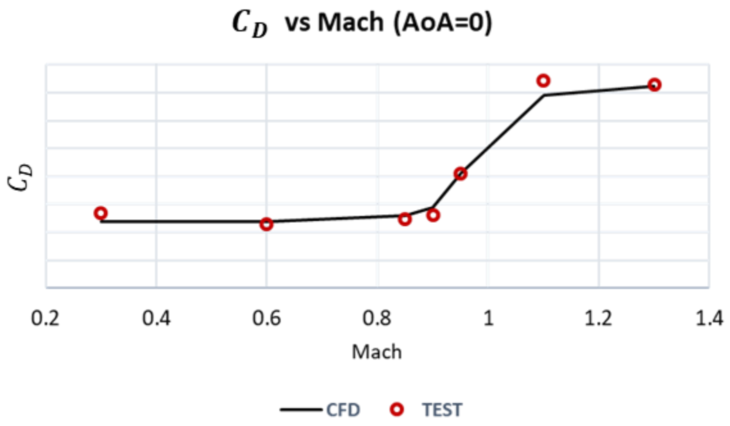

Figure 4.8: Variation of Drag Coefficient

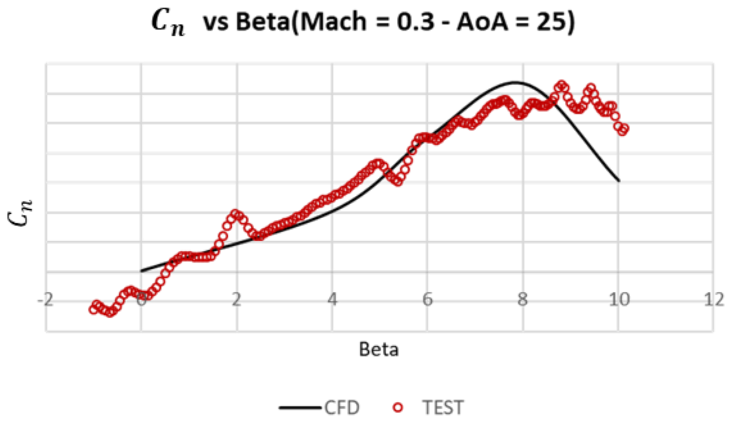

Figure 4.9: Variation of Yaw Moment Coefficient

4.3 Response Surface

The current research focuses on wave drag reduction and directional stability enhancement at take-off and landing configurations. The flow conditions and the objectives of the study are given in Table 4.1. The first objective is to minimize the trim drag at supersonic cruise and second one is to maximize the derivative of yaw moment coefficient with respect to side-slip angle at landing and take-off configurations.

Table 4.1: Flow Conditions used for Objective Function Calculations

Objective	Mach	AoA	Beta
Minimize $C_{D,trim}$	1.2	1.3	0
Maximize C_{n_β}	0.2	25	0-10

4.3.1 Screening Experiments

Before obtaining response surface models for each objective, screening experiments are conducted to determine the significant and insignificant factors. To do that, 2-level factorial (2^k) design is used to generate 16 geometries at the highest and lowest levels of four independent design variables. Then, CFD analyses are conducted on each geometry at the flow conditions given in Table 4.1. Based on Lenth's PSE [31], the significant factors are determined. The Pareto-chart of the standardized effects of 2^k design are provided for objective 1 and objective 2 in Figure 4.10 and Figure 4.11 respectively.

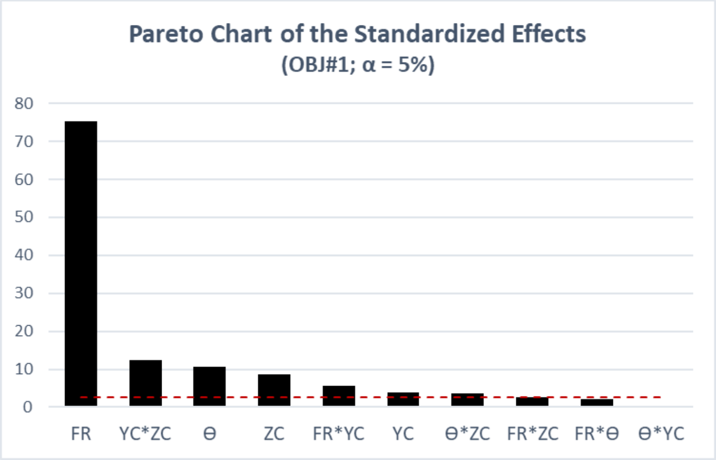

Figure 4.10: Standardized Effects for Objective#1 (2^k-Design)

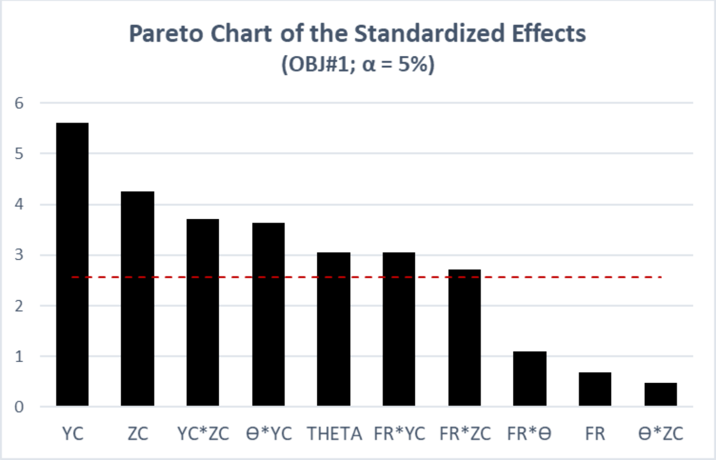

Figure 4.11: Standardized Effects for Objective#2 (2^k-Design)

Based on the screening experiments, all the design variables have significant standardized effects on objective 1. For objective 2, although the fineness ratio has insignificant standardized main effect, its two-way interactions with y and z spline coefficients have significant effect. Hence, the fineness ratio shall be added to the significant factors while conducting response surface analyses. The screening experiments have shown that all the four design variables contribute to both design objectives with a significant amount and the design points could not be further reduced by eliminating any factor.

4.3.2 Three-level Full Factorial Design

Following the completion of screening experiments, using 3-level factorial (3^k) design in which three levels are taken at the minimum, medium and maximum values of each design variable, 81 geometries are produced and for each geometry, CFD analyses are performed at the flow conditions shown in Table 4.1. Once the CFD analyses at the flow conditions shown in Table 4.1 are performed, the objective functions are calculated based on the results obtained from CFD analyses. The CFD results obtained for the first objective function indicates a 1.8% increase in the lift coefficient over the entire design space. Although the change in the lift coefficient is at a negligible amount, the pitch moment coefficient changes by approximately 30% within the entire design space due to the high moment arm of the forebody. Since the pitch moment must be zero in a trim condition, a correction must be applied to the aerodynamic data. The pitching moment change by the forebody design could be balanced by deflecting the horizontal tail. However, this will result in a change in the trim drag. Therefore, a relation between the additional drag coefficient and delta pitch moment coefficient of the horizontal tail must be obtained. The analytical relation between the delta pitch moment coefficient and drag coefficient of the horizontal tail is provided in (4.3). In this relation, the term $C_{D,trim}$ refers to the corrected trim drag coefficient. The terms $C_{D,@\alpha=1.3}$ and $C_{m,@\alpha=1.3}$ are the drag and pitch moment coefficients respectively obtained by the CFD analyses performed at 1.2 Mach, 1.3° of angle of attack and 0° of side slip angle. The terms ΔC_D and ΔC_m are the additional drag and pitch moment coefficients due to horizontal tail deflection. The δ_{HT} term, on the other hand, is the horizontal tail deflection angle. The $\frac{\Delta C_D}{\delta_{HT}}\frac{\delta_{HT}}{\Delta C_m}$ term in (4.3) is obtained by fitting a second order polynomial to $\frac{\Delta C_D}{\delta_{HT}}$ vs $\frac{\Delta C_m}{\delta_{HT}}$ data shown in Figure 4.12.

$$C_{D,trim} = C_{D,@\alpha=1.3} + \frac{\Delta C_D}{\delta_{HT}}\frac{\delta_{HT}}{\Delta C_m} C_{m,@\alpha=1.3} \tag{4.3}$$

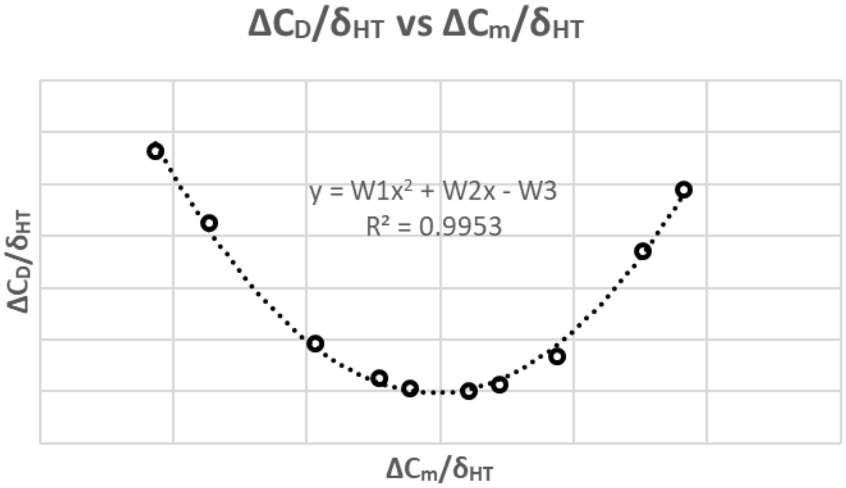

Figure 4.12: Variation of $\frac{\Delta C_D}{\delta_{HT}}$ with $\frac{\Delta C_m}{\delta_{HT}}$

Once the corrections are applied on the trim drag coefficient for the first objective, the effects of design variables with respect to the trim drag coefficient are investigated. In Figure 4.13, the Pareto chart of the standardized effects of the design variables on the first objective is given for a full-quadratic response surface model with a confidence level of 95%. The fineness ratio is the most effective factor for the trim drag coefficient with an almost 10 times higher standardized effect than that of the second most effective parameter, the deflection angle. The remaining parameters, on the other hand, seem to have only a secondary effect for the variation of the first objective. Based on the standardized effects obtained for the first objective, the non-significant effects are removed from the response surface model and a model fit is obtained with a R_{adj}^2 of 99.84% for the trim drag coefficient.

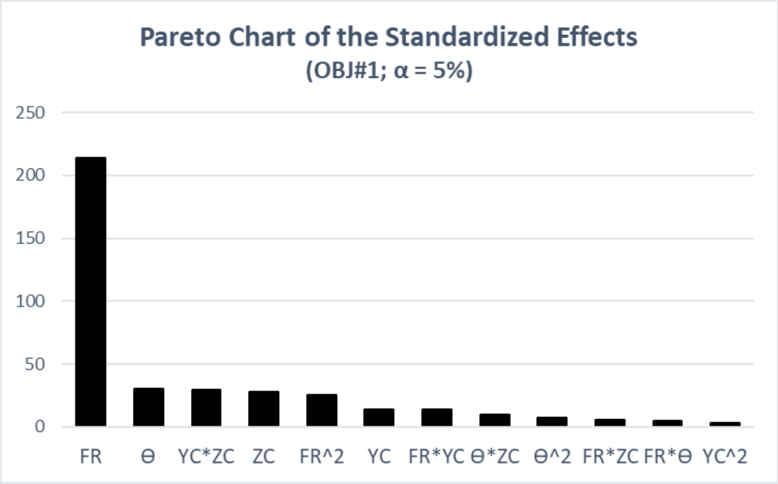

Figure 4.13: Standardized Effects for Objective#1(3^k-Design)

The Pareto chart of the standardized effects of design variables on the second objective, the derivative of yaw moment coefficient with respect to side-slip angle for a full-quadratic response surface model, is provided in Figure 4.14. Based on these results, the second objective is not dominated by a single variable. The y-spline coefficient seems to be the driving factor for the change in directional stability. Following that, nose deflection angle and z-spline coefficient also have a strong main effect on this objective. Again, for the second objective, the non-significant parameters are removed from the relation and a response surface model fit is established with a R_{adj}^2 of 93.71%.

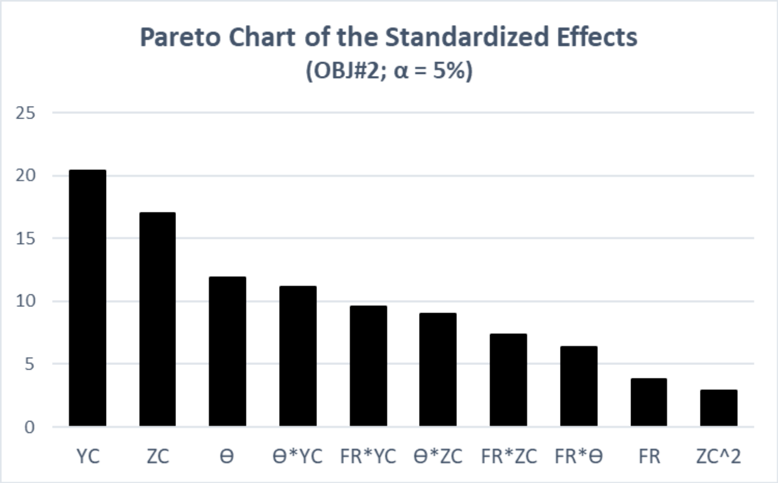

Figure 4.14: Standardized Effects for Objective#2 (3^k-Design)

The previously made model performance assessments are based on a training dataset and do not give an idea about what the model performance would be on an untrained dataset. So, in order to test the model performance on an untrained dataset, 8 random geometries which correspond to the 10% of the geometries used in the training dataset are generated. Then, the CFD analyses stated in Table 4.1 are performed on these geometries. The geometries in the test dataset are displayed in Figure 4.15.

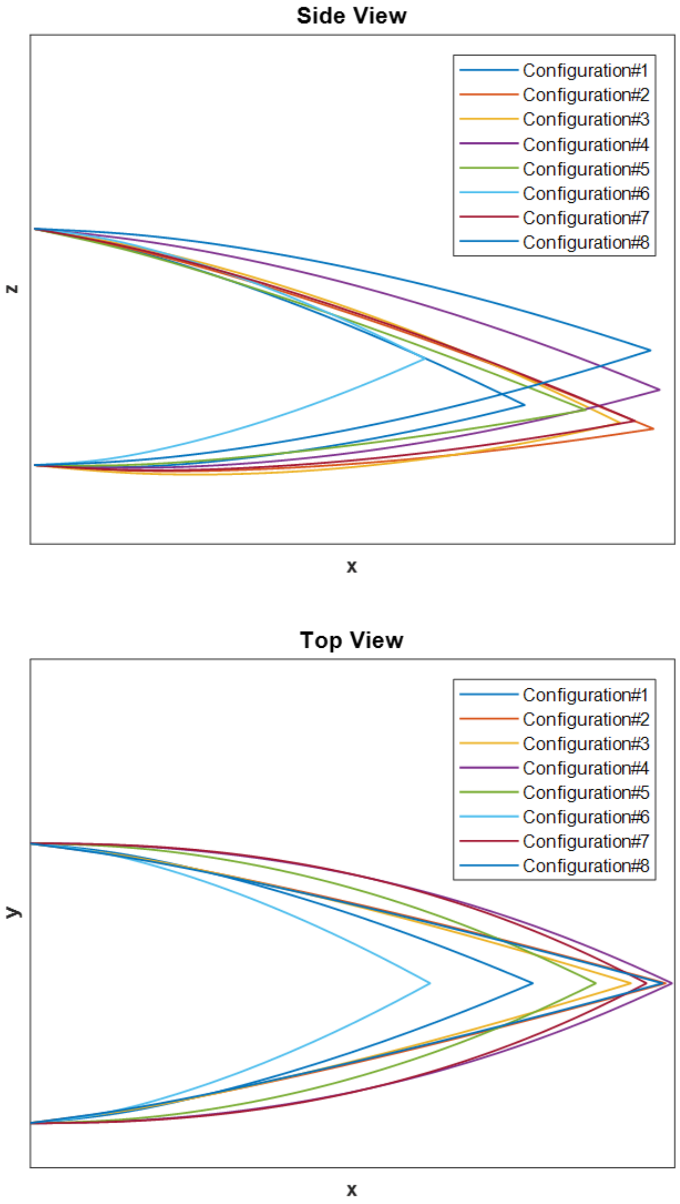

Figure 4.15: Sample Geometries in the Test Dataset

After the verification of SU2 solutions, the predictions of response surface models for both objectives are compared to the ones obtained from the SU2 solutions. By considering the CFD results as the true values of the objectives, the prediction errors of the response surface model are obtained for the test dataset and provided in Table 4.2. The terms ε_{CD} and $\varepsilon_{CN\beta}$ in Table 4.2 are the percent prediction errors for the first and second objective response surface models respectively. Based on the prediction errors of the first objective, it can be stated that highly accurate results are obtained for the prediction of the trim drag coefficient. The largest error for this objective is 0.11%. The main reasons behind such small errors are that the drag coefficient changes by 6.5% at most in the entire design space and the dominating factor, fineness ratio, forms almost a linear relation with the trim drag coefficient. The predictions of the response surface model for the second objective, on the other hand, have higher error compared to that of the first objective. However, while evaluating the error terms in the second objective predictions, it should be noted that the yaw moment coefficient changes by 77% in the entire design space.

Table 4.2: Test Dataset Error

$Geometry$	ε_{CD}	$\varepsilon_{CN\beta}$
1	0.11%	0.40%
2	0.07%	3.38%
3	0.07%	0.71%
4	0.00%	2.82%
5	0.02%	1.74%
6	0.03%	0.52%
7	0.04%	2.89%
8	0.01%	3.96%

The variation of design objectives with respect to design variables are provided in Figure 4.16 and Figure 4.17 for objective 1 and 2 respectively. The trim drag in the first objective decreases with increasing fineness ratio, nose deflection angle and y-spline coefficient. On the other hand, the trim drag increases with increasing z-spline coefficient. The yawing moment derivative with respect to side-slip angle exhibits a linear increment with increasing fineness ratio and y-spline coefficient. However, a decrease is observed in the directional stability indicator while increasing nose deflection angle and z-spline coefficient. One should note that, the sensitivity plots are obtained by changing a single parameter at a time while others are kept constant. Therefore, the interaction effects cannot be deducted from these graphs.

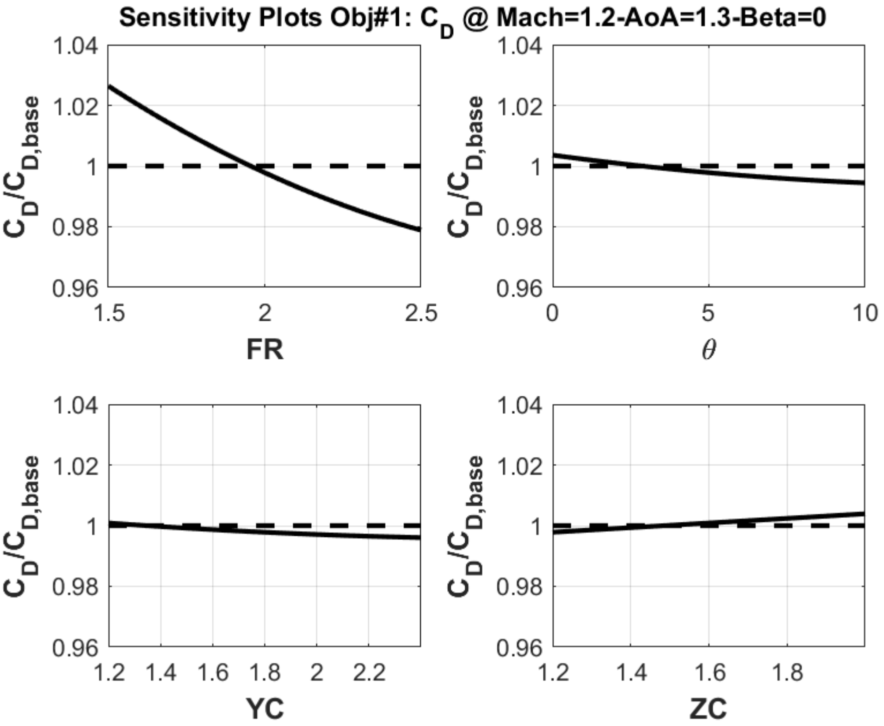

Figure 4.16: Sensitivity Plots for Objective #1

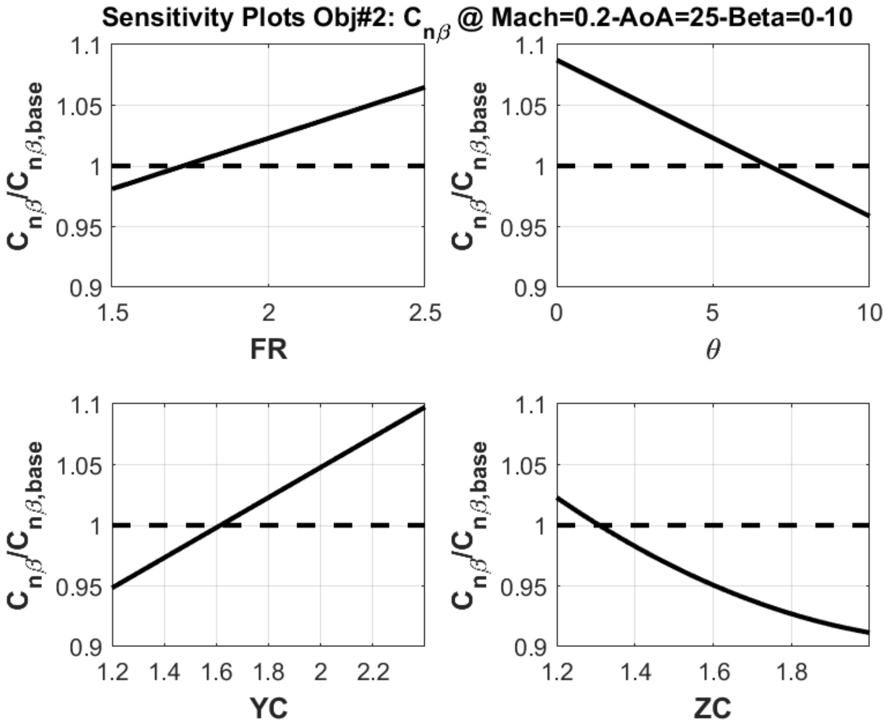

Figure 4.17: Sensitivity Plots for Objective #2

4.4 Pareto Optimal Solutions

After obtaining the RSM regression coefficients for each objective, the entire design space is searched for Pareto-optimal solutions with NSGA-II. Before doing that, the optimal values of each objective are searched by the classical genetic algorithm separately since NSGA-II requires more than one objective to conduct non-dominated sorting. While doing so, the population size, crossover probability, and mutation rate are set to 20, 0.7, and 0.02 respectively. The first investigation is conducted on the minimum value of trim drag coefficient. The variation of trim drag coefficient relative to the base configuration's trim drag coefficient with the iteration count and the best drag configuration are provided in Figure 4.18. A convergence is achieved within approximately 60 iterations. An approximately 2.1% improvement on the baseline configuration's trim drag coefficient is observed by the best drag configuration.

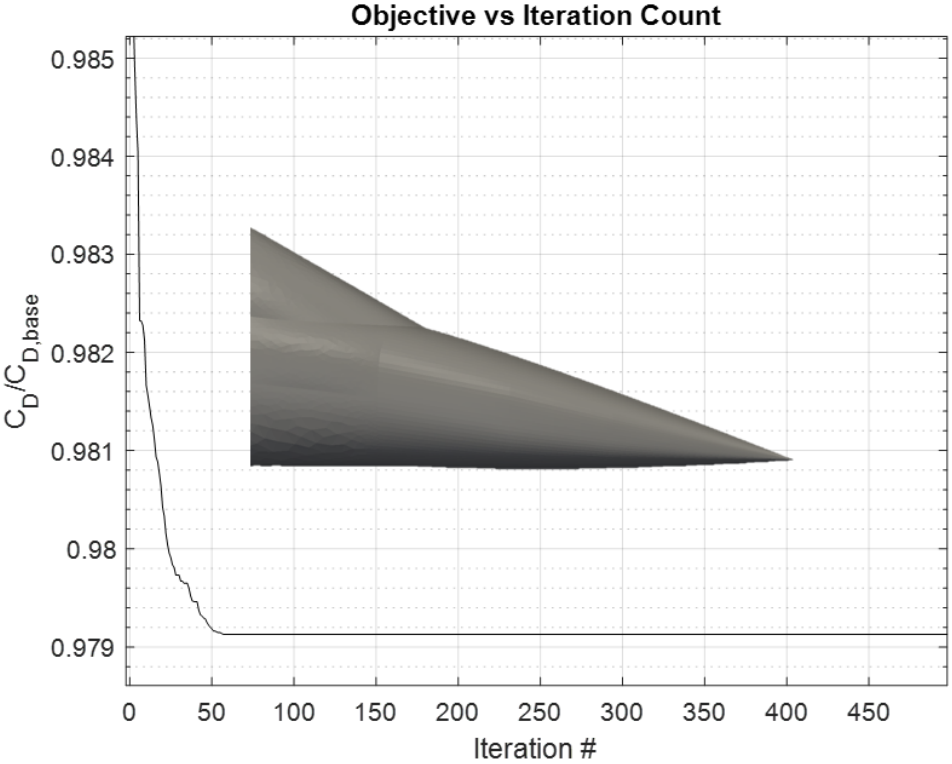

Figure 4.18: Variation of Objective #1 and the Best Drag Configuration

The maximum value of the second objective, the yawing moment derivative with respect to side-slip angle, is searched again by using the classical genetic algorithm. The variation of the second objective relative to the base configuration's yawing moment derivative with the iteration count and the best directional stability configuration are provided in Figure 4.19. The convergence to the maximum value is achieved around 40 iterations. The directional stability of the baseline configuration at 0.2 Mach, 25 degrees of angle of attack may be increased by approximately 30% by the best directional stability configuration.

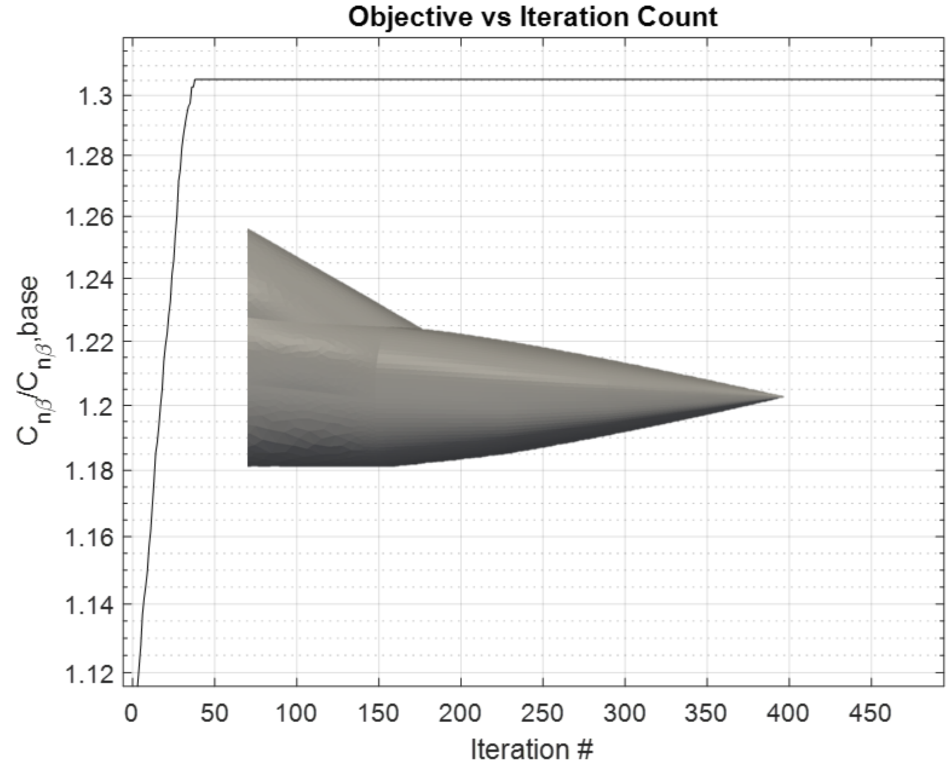

Figure 4.19: Variation of Objective #2 and the Best Directional Stability Configuration

When performing the Pareto-optimal search analyses with NSGA-II, the population size, crossover probability, and mutation rate are set to 20, 0.7, and 0.02 respectively as used in the classical genetic algorithm. In Figure 4.20, the final Pareto-front solutions obtained by NSGA-II are represented by the red circles whereas the black circles represent the initial population generated at the beginning of this iterative procedure. In this graph, the horizontal axis indicates the value of the first objective function relative to the base configuration in an ascending order from left to right and the vertical axis indicates the value of the second objective function relative to the base configuration in an ascending order from bottom to top. The domination of Pareto-front solutions over the initial population can be clearly seen in this graph.

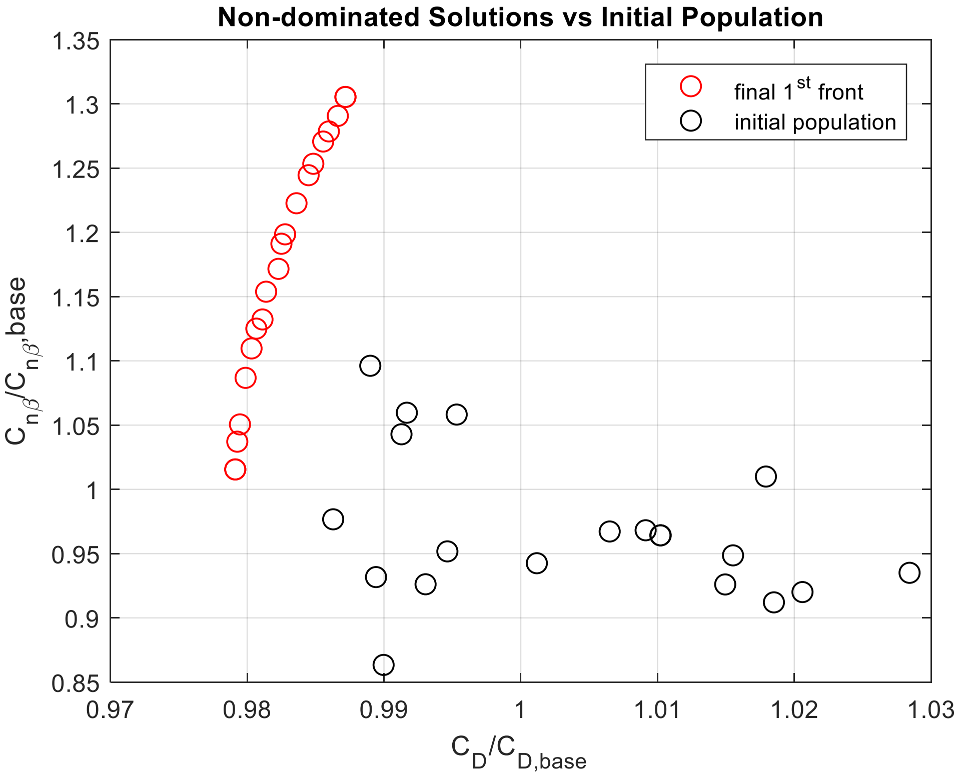

Figure 4.20: Pareto-Optimal Solutions vs Initial Population

In Figure 4.21, the variation of minimum drag coefficient and highest yaw moment coefficient ever evaluated in the population relative to the base configuration with the iteration count are shown. The convergence for the trim drag coefficient is achieved approximately around 350 iterations whereas it is approximately 210 iterations for yaw moment coefficient derivative. Note that the convergence achieved by NSGA-II requires more iterations compared to the classical single objective genetic algorithm. However, NSGA-II provides a Pareto-optimal set of solutions with the same size of population whereas the classical genetic algorithm provides a single solution.

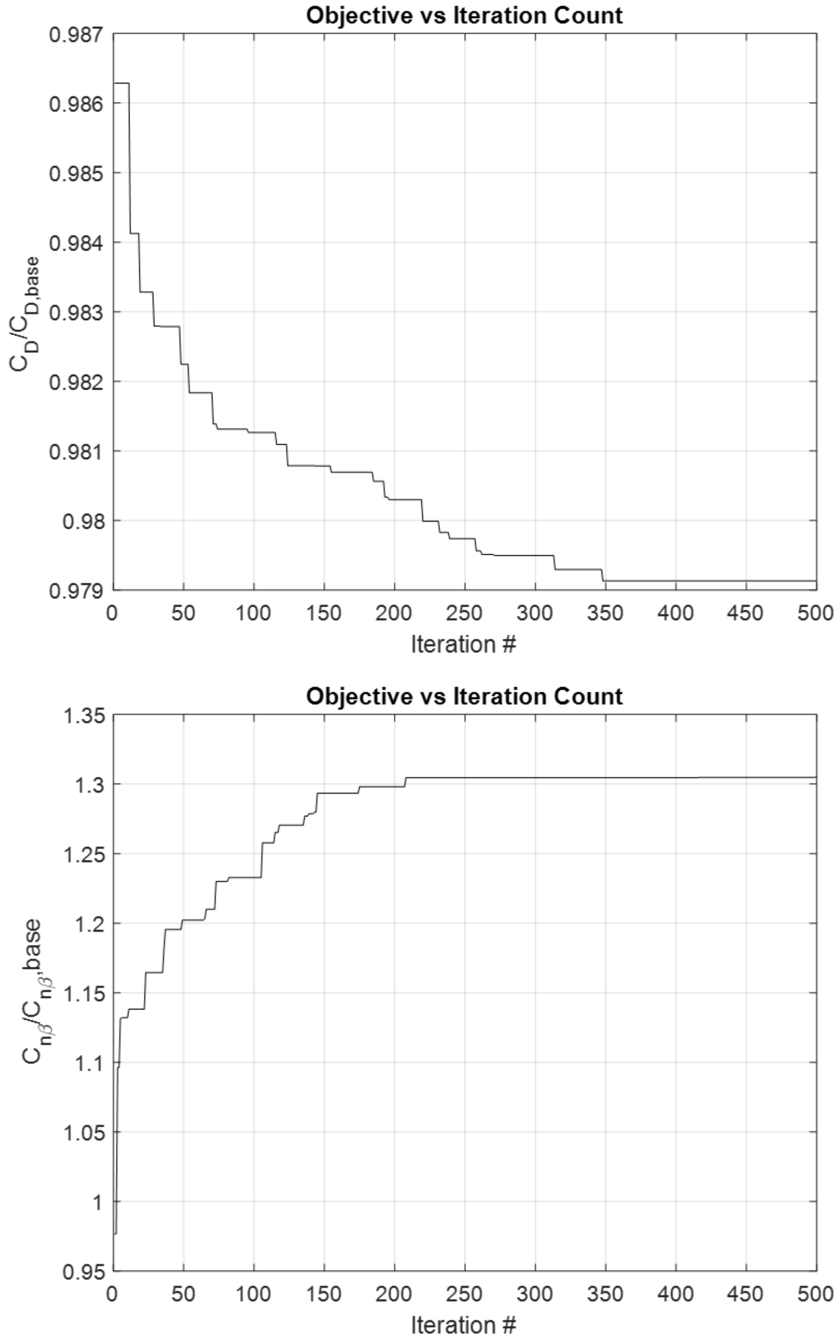

Figure 4.21: Objectives vs Iteration Count

Figure 4.22 shows the variation of design variables FR, θ, YC and ZC with respect to the iteration count. The variations of configurations are given for each objective function separately. For both objectives, the FR value converges to 2.5 and this behavior is coherent with screening experiment results. The design variable θ, on the other hand, exhibits an opposite behavior for each objective. The θ value converges to 10° for the minimum drag configuration whereas a convergence to 0° of θ is observed for the best directional stability configuration. The YC converges to a moderate value of 2.1 for the minimum drag configuration. The best directional stability configuration is obtained with a YC value converging to 2.4 which is the maximum value of YC in the design space. The ZC, similar to FR, converges to the same value of 1.2 for both objectives as indicated by screening experiment results.

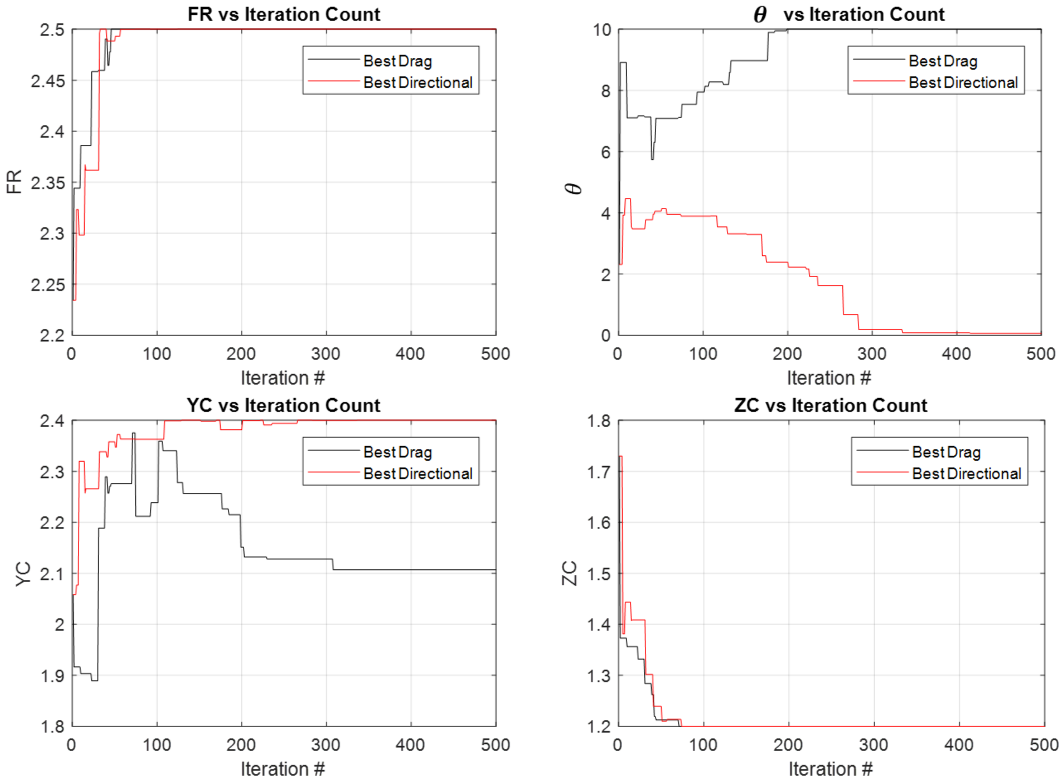

Figure 4.22: Variation of Design Variables: FR (Top-Left), θ (Top-Right), YC (Bottom-Left) and ZC (Bottom-Right)

NSGA-II searches for Pareto-optimal solutions by inserting the objective functions separately. The classical genetic algorithm, on the other hand, requires a single objective which might be obtained by attaining weights to the objective functions. In order to compare the Pareto-optimal results obtained by NSGA-II with the ones obtained by classical genetic algorithm, a Pareto-optimal search is conducted on a single objective by attaining weights to the objective functions for 20 times, which is the population size used in NSGA-II. The results are displayed in Figure 4.23. As observed, the Pareto-optimal solutions obtained by both algorithms lie in the same Pareto-optimal curve. However, the positions of the individuals in the design space are not the same for each individual obtained by both algorithms. The reason behind that is the randomness of NSGA-II. Since NSGA-II is a random search algorithm, depending on the population size, there might be slight changes in the position of optimal solutions on the Pareto-optimal curve. Note that the Pareto-optimal configurations with the best drag and the best directional stability configurations are the same with the ones obtained by the classical genetic algorithm.

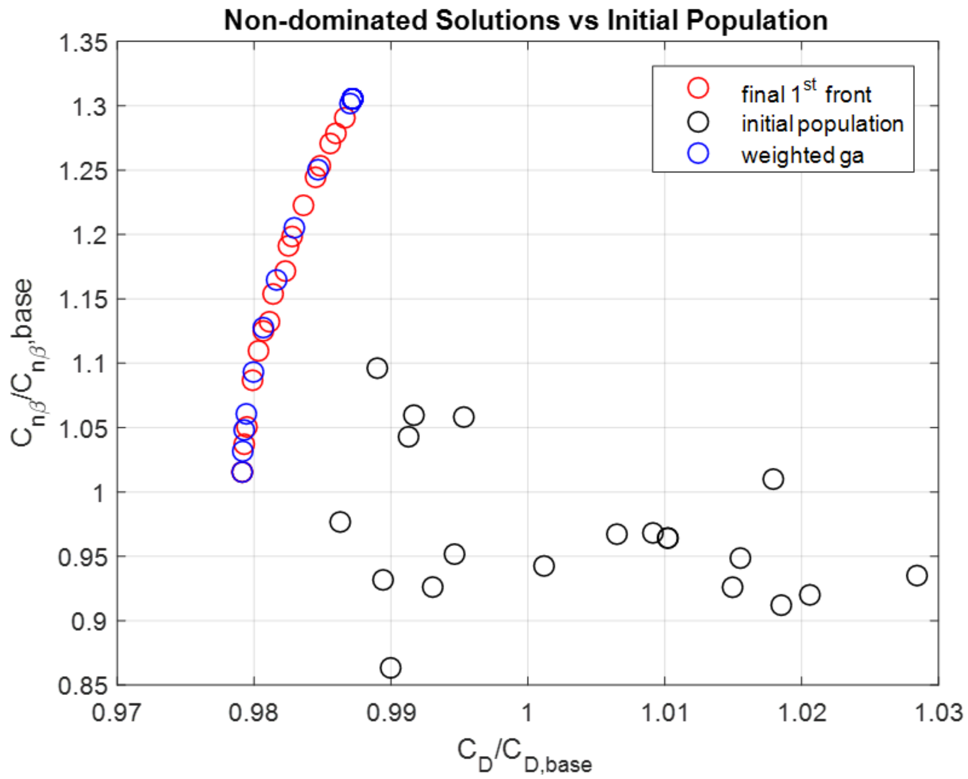

Figure 4.23: Comparison of NSGA-II results with Weighted Genetic Algorithm

Three different configurations are chosen from the Pareto-optimal solution set and the SU2 analyses given in Table 4.1 are performed for these three geometries. The Figure 4.24 shows the Mach number distribution over two different slices taken at y

= 0 and z-coordinate corresponding to the forebody apex of each of the three geometries chosen from Pareto-front solutions for the case with 1.2 Mach number, 1.3° of angle of attack and 0°of side slip angle. The one on the top of this figure has the highest directional stability, the one to middle has the lowest wave drag and the bottom one has the moderately low wave drag and high directional stability compared to the baseline model.

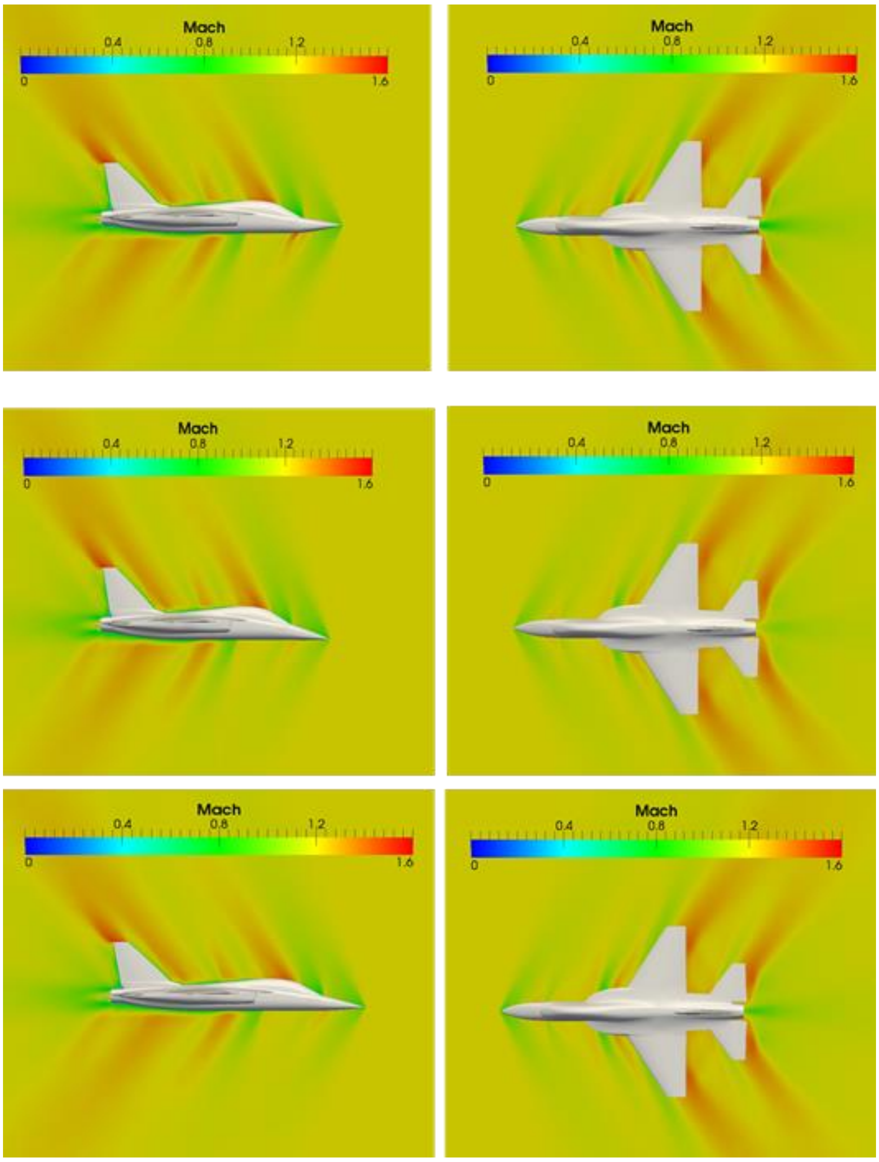

Figure 4.24: Mach number Distribution over the Best Directional Stability Configuration (Top), Lowest Drag Count Configuration (Middle), Moderately Optimal Configuration (Bottom)

To investigate the shock characteristics of the selected Pareto-optimal configurations, the shock angles of the oblique shock occurring at the forebody apex are approximately measured. These angles are provided in Figure 4.25 for the base (top-left), best directional stability (top-right), best drag (bottom-left) and moderately optimal (bottom-right) geometries. The highest shock angles are observed in the base geometry. For the best drag geometry, although the shock angle on the upper side of the forebody is high, the one on the bottom side is significantly decreased with the forebody design. Similarly, the shock angle on the bottom side of the moderately optimal forebody is reduced significantly. On the other hand, a noteworthy decrease only in the upper side shock angle is observed for the best directional stability geometry.

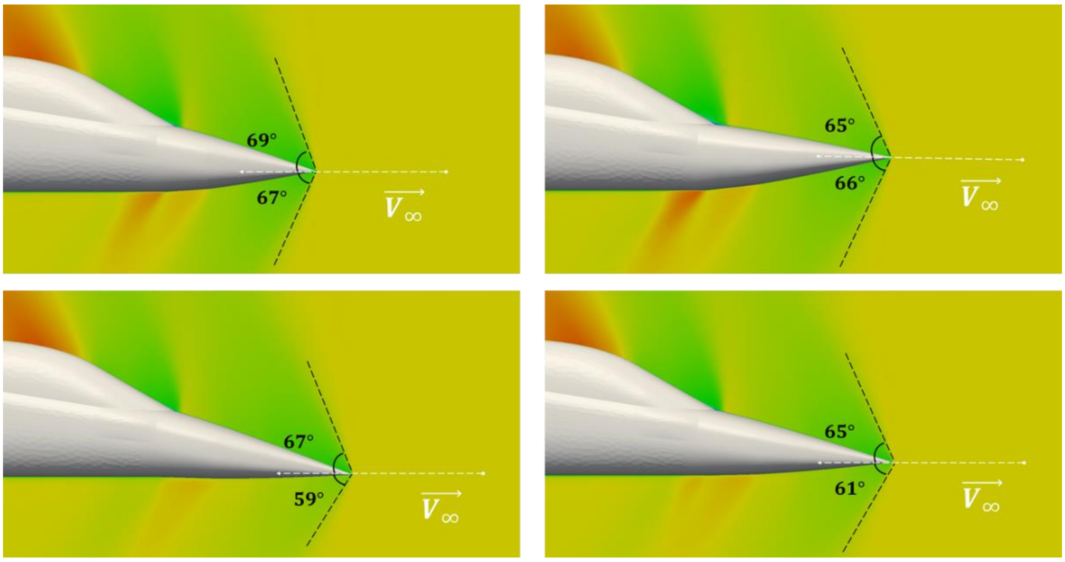

Figure 4.25: Shock Angles over the Base Configuration (Top-Left), Best Directional Stability Configuration (Top- Right), Lowest Drag Count Configuration (Bottom-Left), Moderately Optimal Configuration (Bottom- Right)

In Figure 4.26, the pressure coefficient distributions over the base and three Pareto-optimal configurations are provided. Since the length of the geometries differ in x-direction, the horizontal axis in this graph represents the non-dimensional x distance. A value of 0 in non-dimensional x distance corresponds to the forebody tip and a value of 1 in non-dimensional x distance corresponds to the forebody end. The base configuration has the largest pressure coefficient values on both upper and lower surfaces. Apart from that, the best drag configuration has similar pressure distribution on the upper surface with the base configuration. The pressure distribution on the lower surface, on the other hand, is quite lower compared to the base configuration. However, the pressure coefficient difference in the upper and lower surfaces of the best drag configurations causes a higher lift force on the forebody geometry which eventually causes higher pitching moment difference from that of trim condition. The change in the pitching moment would cause a downgrade on the improvement of trim drag. The best directional stability configuration also has lower pressure coefficient distributions on both surfaces compared to the base configuration. In addition to that, since the pressure difference between the upper and lower surface of the best directional stability configuration is low, it will create less pitching moment deviations from the trim condition which may bring additional improvement to the trim drag. For the moderately optimal configuration, the pressure distribution on the upper surface is lower compared to the best drag configuration. However, the one on the upper surface of the moderately optimal configuration is higher compared to the best drag configuration. The pressure difference between the upper and lower surfaces of the moderately optimal configuration is also lower compared to the best drag configuration. This indicates a lower additional drag caused by the pitching moment for the moderately optimal configuration compared to the best drag configuration. Based on the pressure distributions shown in Figure 4.26, a strong shock formation is observed in the vicinity of the forebody-canopy junction. The highest pressure increase is observed in the best directional stability configuration. The reason behind this is that the best directional stability configuration has the lowest nose deflection angle among the configurations shown in Figure 4.25 which causes a higher angle in the forebody-canopy junction which eventually causes stronger shock formation. The lowest pressure increase is observed in the best drag configuration contributing to the wave drag increase less than the other three contributions. For the base and moderately optimal configurations, similar pressure increase is observed in the forebody-canopy junction.

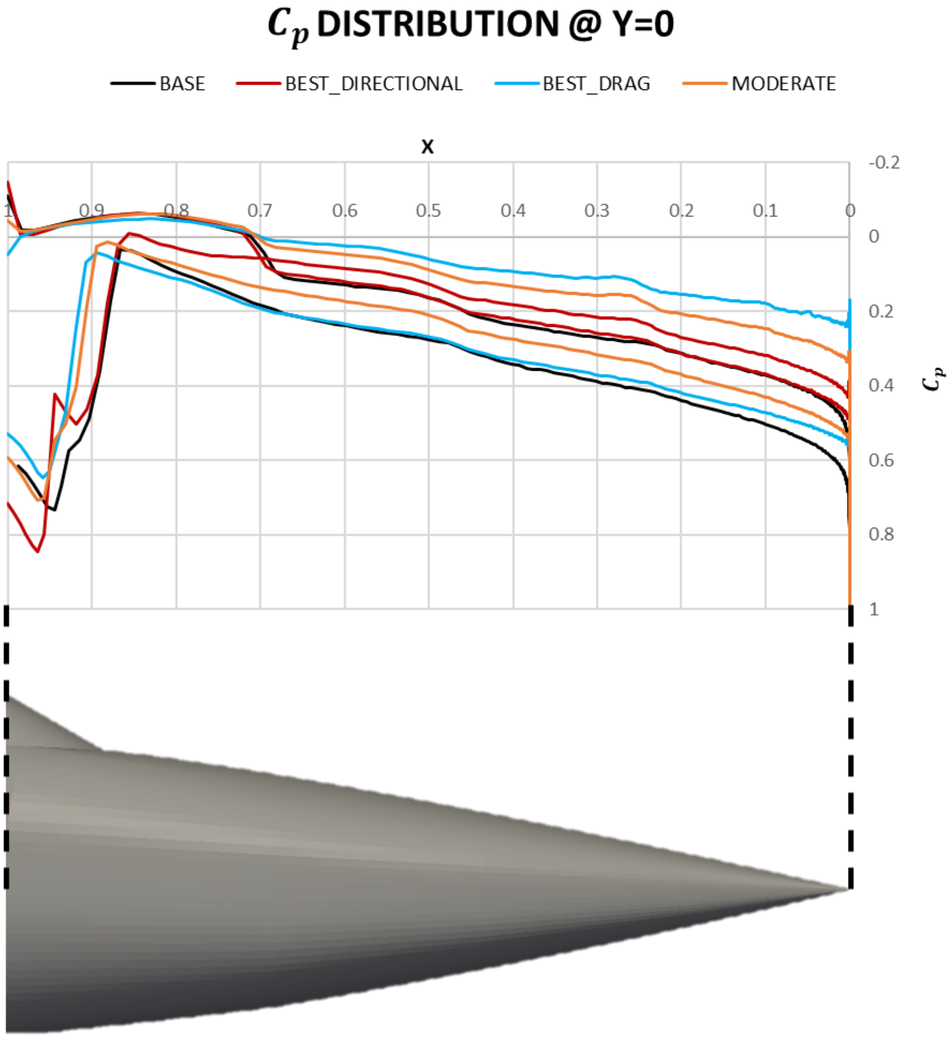

Figure 4.26: Pressure Coefficient Distributions over the Base Configuration (Top-Left), Best Directional Stability Configuration (Top- Right), Lowest Drag Count Configuration (Bottom-Left), Moderately Optimal Configuration (Bottom- Right) @ Y=0

The drag coefficients of the base and three Pareto-optimal configurations are decomposed into pressure and friction components in SU2 solutions and their percentages are provided in Figure 4.27. The pressure component, which also includes the wave drag component, has the lowest percentage in the best drag and moderately optimal configurations.

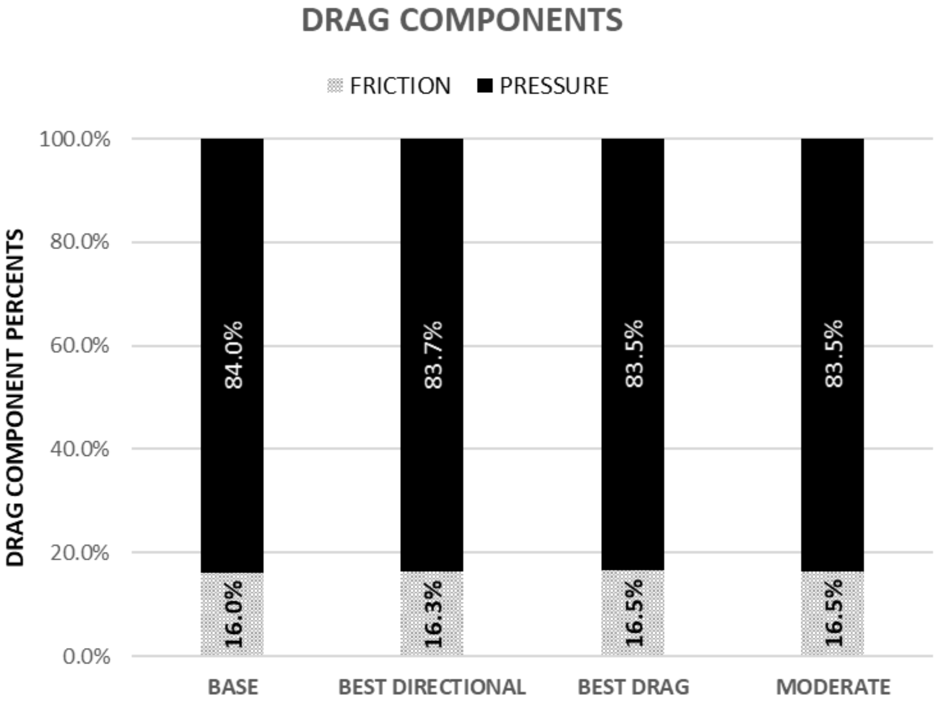

Figure 4.27: Drag Component Percentages for the Base, Best Directional Stability and Moderately Optimal Configurations

Recall that for an isentropic flow, the relation between the total pressure and static pressure could be obtained by using the formula given in (4.4).

$$\frac{p_0}{p} = \left(1 + \frac{\gamma - 1}{2} M^2\right)^{\frac{\gamma}{\gamma - 1}} \qquad (4.4)$$

Based on this formulation, a term called “isentropic Mach number” could be obtained. This term enables users to obtain Mach number distribution over the surfaces by assuming that the total pressure is preserved within the flow domain. However, in the presence of shockwaves and a viscous phenomenon within the boundary layer, there is going to be certain losses in the total pressure. Therefore, the Mach distribution obtained on the surfaces is provided by an error margin due to isentropic flow assumption. Yet, the isentropic Mach number may give an idea about the locations where the flow is accelerated, and the shock-induced separations occurred. The formulation of isentropic Mach number is provided in (4.5).

$$\begin{aligned} M_{isentropic} &= \sqrt{\left(\frac{p_0}{p}\right)^{\frac{\gamma-1}{\gamma}} \frac{2}{\gamma-1} - 1} \\ &= \sqrt{\left(\frac{p_\infty}{p}\right)^{\frac{\gamma-1}{\gamma}} \left(1 + \frac{\gamma-1}{2} {M_\infty}^2\right) \frac{2}{\gamma-1} - 1} \end{aligned} \tag{4.5}$$

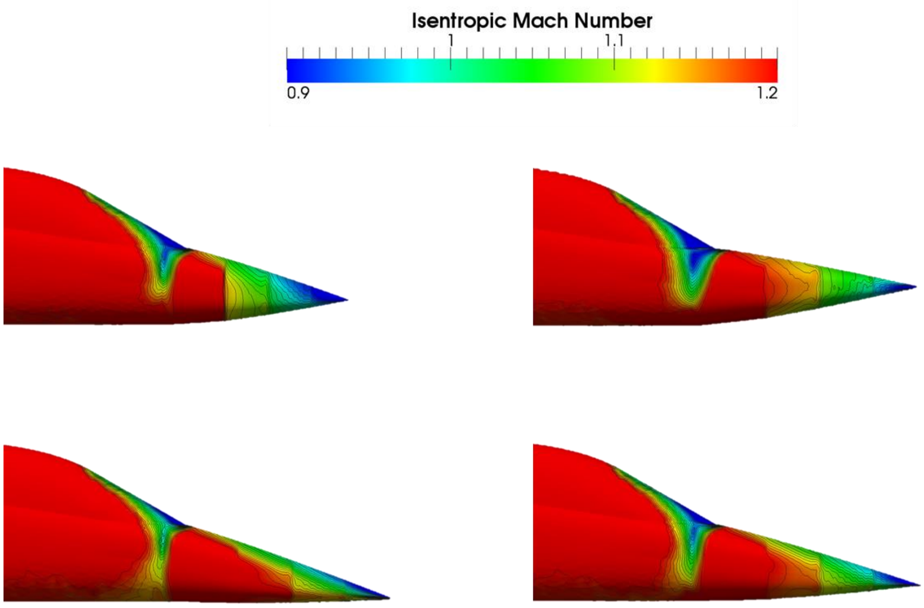

Figure 4.28: Isentropic Mach number Distribution over the Base Configuration (Top-Left), Best Directional Stability Configuration (Top- Right), Lowest Drag Count Configuration (Bottom-Left), Moderately Optimal Configuration (Bottom-Right)

In Figure 4.28, the isentropic Mach number distribution over the base and three Pareto-optimal configurations are given in a side view. It is possible to observe that the accelerated flow region covers a greater space on the forebody geometry for the best drag and moderately optimal configurations compared to the base and best directional stability configurations. The accelerated flow regions indicate a lower pressure over the surface and less contribution to the drag force.

Figure 4.29 shows the streamlines passing through the apex of the forebody for the three Pareto-optimal solutions to better understand the effect of forebody geometry on directional characteristics. The streamlines are spread out more in the geometry with the lowest directional stability, whereas the streamlines are more concentrated in the geometry with the highest directional stability.

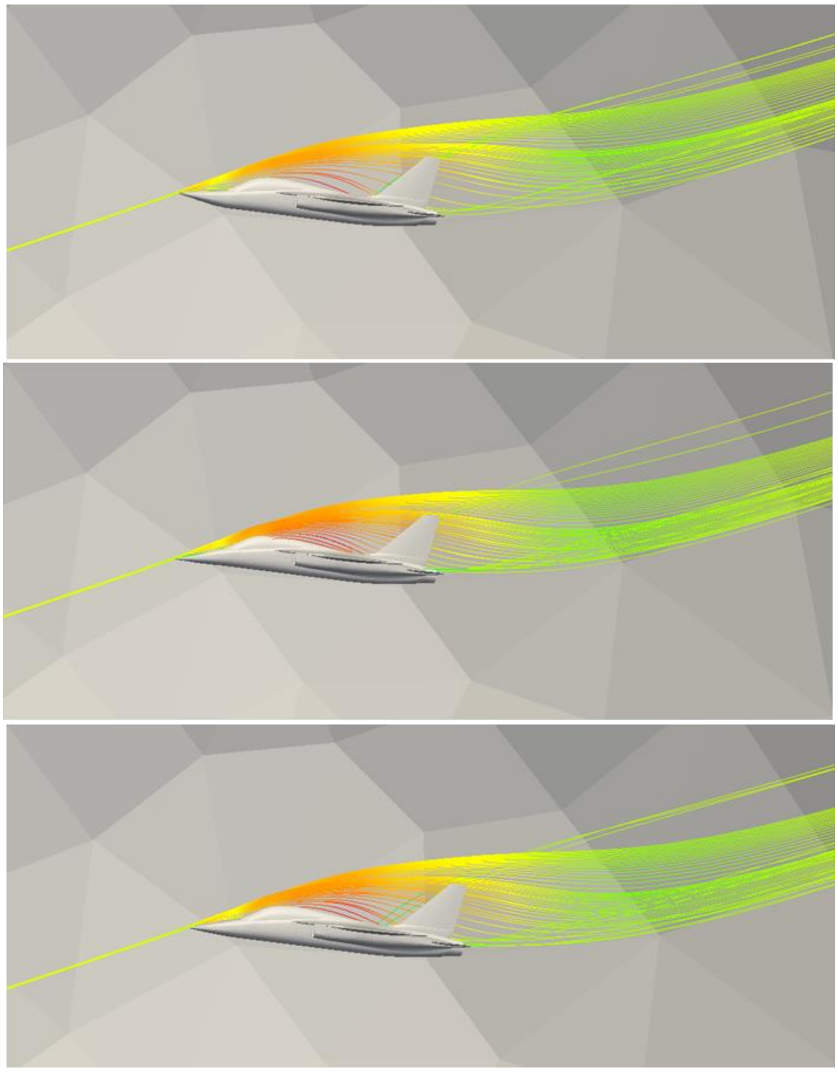

Figure 4.29: Streamlines over the Best Directional Stability Configuration (Top), Lowest Drag Count Configuration (Middle), Moderately Optimal Configuration (Bottom)

In Figure 4.30 and Figure 4.31, Q-criterion iso-surfaces (Q=0.01) for 0.2 Mach, 25 degrees of angle of attack and 10 degrees of side-slip angle flow solutions over the three Pareto-optimal geometries and the base geometry are provided. Q refers to the second invariant of the velocity gradient tensor and is commonly used for the visualization of vortex structures in the flow. One may observe from these figures, the vortex structures emanating from the apex of the forebody are denser for the forebody with the best directional stability. Following that, the moderately optimal forebody has the second highest dense vortex structure. For the base and best drag geometries, a less dense vortex structure emanates from the forebody apex. The results are coherent with Witford’s [7] statements. Nonetheless, the vortex structures emanating from the forebody apex seem to fade out before reaching to the vertical tail.

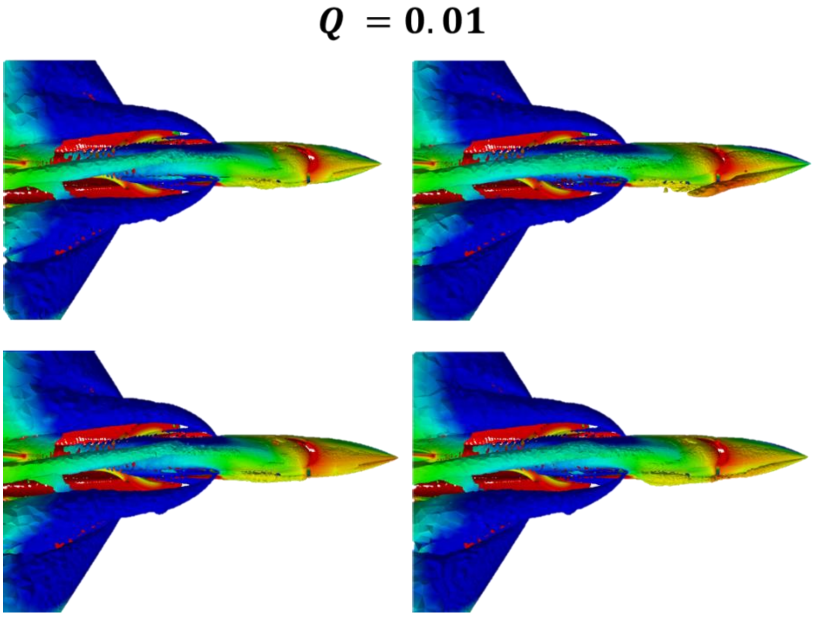

Figure 4.30: Q-criterion Iso-surfaces (TOP-VIEW) @ (0.2 Mach - 25°- AoA - 10° Beta) over the Base Configuration (Top-Left), Best Directional Stability Configuration (Top- Right), Lowest Drag Count Configuration (Bottom-Left), Moderately Optimal Configuration (Bottom- Right)

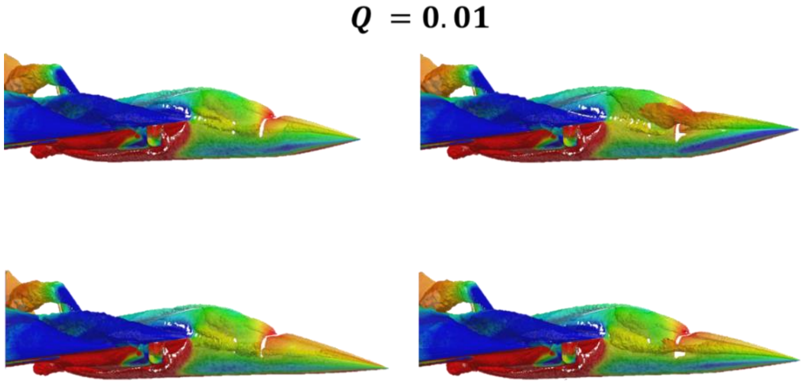

Figure 4.31: Q-criterion Iso-surfaces (SIDE-VIEW) @ (0.2 Mach - 25°- AoA - 10° Beta) over the Base Configuration (Top-Left), Best Directional Stability Configuration (Top- Right), Lowest Drag Count Configuration (Bottom-Left), Moderately Optimal Configuration (Bottom- Right)

Table 4.3 shows the RSM predictions as well as the CFD-provided actual improvements on each objective. Based on the CFD results, the best drag geometry predicted by the response surface models appears to be dominated by the moderate geometry, as both geometries provide the same performance for objective 1, but the moderate geometry provides better directional characteristics. As a result, the best drag geometry is no longer among the Pareto-optimal solutions.

Table 4.3: Objective Improvements on the Selected Geometries (Predicted / Actual)

Geometry	Minimize $C_{D,trim}$	Maximize C_{n_β}
Best Directional Stability	1.3% / 1.3%	30.5% / 33.0%
Best Drag	2.1% / 2.0%	1.5% / 0.8%
Moderate	1.9% / 2.0%	12.8% / 14.6%

Since the best drag geometry is no longer in the Pareto-optimal configurations, the characteristics of best directional stability and moderately optimal geometries could be further investigated. As Chambers [8] stated, the strong vortex formation at the forebody apex for high angle of attack flows may cause flow asymmetries.

Therefore, an investigation is conducted on the yawing moment coefficient at 0.2 Mach, 25 degrees of angle of attack and 0 degree of side-slip angle of base and two Pareto-optimal geometries and the data is provided in Figure 4.32. The yawing moment coefficients are normalized using the base geometry's yawing moment coefficient and the absolute values of the yawing moment coefficient are used.

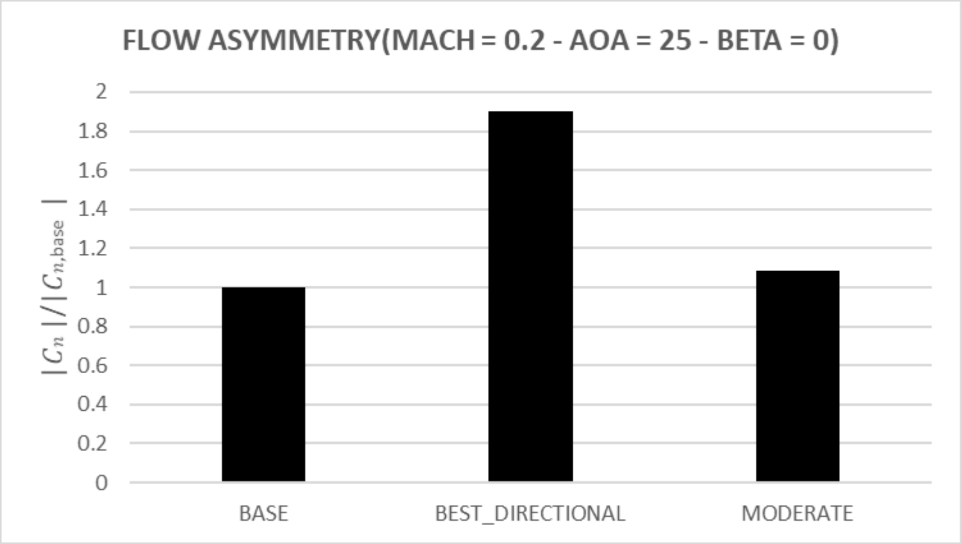

Figure 4.32: Flow Asymmetry Data for Base and Two-Pareto Optimal Configurations

The results have yielded that the flow asymmetry in the best directional configuration causes a yawing moment coefficient almost twice that of base configuration. On the other hand, the asymmetries present in the moderately optimal configuration cause only a 10% increase compared to the base configuration.

To investigate the reason behind the flow asymmetries, the Q-criterion iso-surface are obtained with a Q-value of 0.01 and given in Figure 4.33 for the base, best directional stability and moderately optimal configurations. As observed the densest vortex formation occurs in the best directional stability configuration and the statements of Chamber [8] on the relation between the vortex strength and flow asymmetries seem to be observed in SU2 solutions as well.

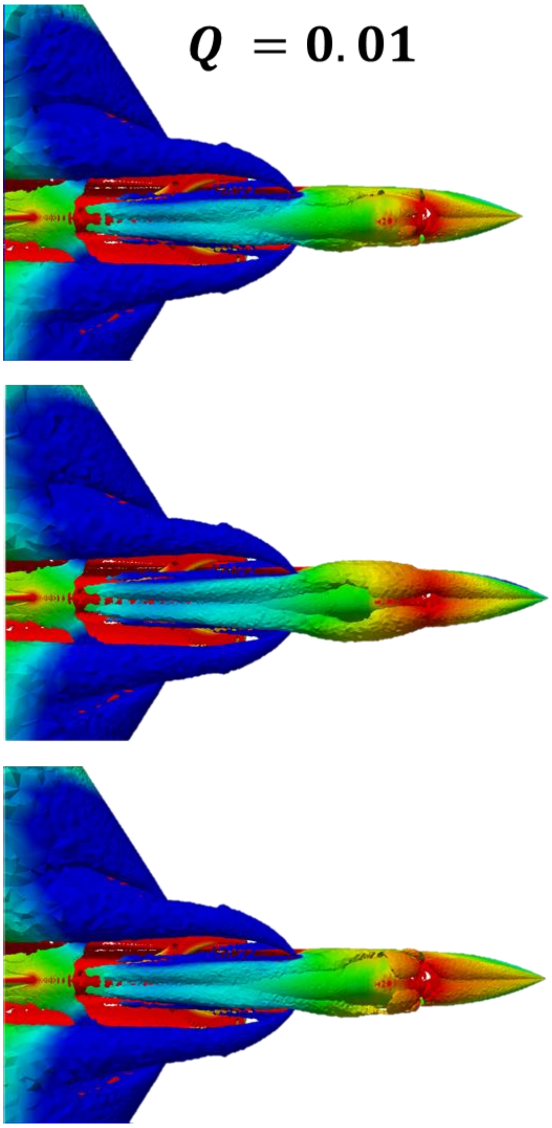

Figure 4.33: Q-criterion Iso-surfaces (TOP-VIEW) @ (0.2 Mach - 25°- AoA - 0° Beta) over the Base Configuration (Top), Best Directional Stability Configuration (Middle), Moderately Optimal Configuration (Bottom)

CHAPTER 5

CONCLUSION

In this thesis, an optimization study has been conducted on the forebody geometry of a jet trainer aircraft to improve its supersonic cruise performance and directional stability characteristics. To represent the lateral cross-section of the forebody geometry, four independent design variables are used. Response Surface Method is used for optimization, and the aerodynamic database for the objective functions is generated by means of turbulent flow solutions with SU2. Based on response surface models, NSGA-II is used to search for Pareto-optimal solutions.

The present optimization study conducted on the forebody optimization provides promising improvements on the wave drag and directional stability. The driving factor in the reduction of wave drag is the fineness ratio, and the wave drag is reduced by producing high fineness ratio forebodies with low z-spline coefficient. A similar pattern is observed in the improvement of directional stability. The two objectives contradict each other while changing the forebody deflection angle and y-spline coefficient. The aircraft's directional stability decreases with increasing deflection angle and decreasing y-spline coefficient, whereas the opposite behavior is observed in the wave drag.

It is concluded that a significant improvement in the directional stability and an unignorable decrease in the wave drag can be achieved with a proper forebody design. As future work, the yaw moment coefficient may be included among the objective function to be investigated in more detail.

REFERENCES

[1] Anderson, J. D. “Compressible Flow: Some Preliminary Aspects.” Essay. In Fundamentals of Aerodynamics, 5th ed., 516. London: Mcgraw-hill Publishing Co., 2007.

[2] Davies, Peter E., Jim Laurier, Gareth Hector, and Tony Holmes. “Introduction.” Essay. In X-Planes. Bell X-1, 5. United Kingdom, Oxford: Osprey, 2016.

[3] Schneider, Wolfgang. “The Importance of Aerodynamics in the Development of Commercially Successful Transport Aircraft.” Aerodynamic Drag Reduction Technologies, 2001, 9–16.

[4] Daniel P. Raymer, “Aircraft Design: A Conceptual Approach”, 155. Washington, D.C, AIAA, 1989.

[5] Al-Obaidi, Abdulkareem Sh. Mahdi, and Mushtak Al-Atabi. “Effect Of Body Shape on The Aerodynamics of Projectiles at Supersonic Speeds.” Journal of Engineering Science and Technology 3 (December 2008).

[6] Daniel P. Raymer, “Aircraft Design: A Conceptual Approach”, 157. Washington, D.C, AIAA, 1989.

[7] Whitford, Ray. Design for Air Combat. Delft: TU Delft, 2014.

[8] J. R. Chambers, E. L. Anglin and J. S. Bowman, "Effects of a Pointed Nose on Spin Characteristics of a Fighter Airplane Model Including Correlation with Theoretical Calculation," Langley Research Center, Hampton, 1970.

[9] Ganguli, Ranjan, and S Rajagopal. “Multidisciplinary Design Optimization of an UAV Wing Using Kriging Based Multi-Objective Genetic Algorithm.” 50th AIAA/ASME/ASCE/AHS/ASC Structures, Structural Dynamics, and Materials Conference, 2009.

[10] Yamamoto, Kenji, and Osamu Inoue. “Applications of Genetic Algorithm to Aerodynamic Shape Optimization.” 12th Computational Fluid Dynamics Conference, 1995.

[11] Antunes, Alexandre P., and João Luiz Azevedo. “Studies in Aerodynamic Optimization Based on Genetic Algorithms.” Journal of Aircraft, vol. 51, no. 3, 2014, pp. 1002–1012.

[12] Chen, Xiaomin, and Ramesh K. Agarwal. “Optimization of Wind Turbine Blade Airfoils Using a Multi-Objective Genetic Algorithm.” Journal of Aircraft, vol. 50, no. 2, 2013, pp. 519–527.

[13] Sakaoğlu, Sergen, and Harika Senem Kahveci. “The Influence of Cooling Configuration and Tip Geometry on Gas Turbine Blade Tip Leakage Flow and Heat Transfer,” 2019.

[14] Economon, Thomas D., et al. “SU2: An Open-Source Suite for Multiphysics Simulation and Design.” AIAA Journal, vol. 54, no. 3, 2016, pp. 828–846.

[15] Spalart P., and S. Allmaras. “A One-Equation Turbulence Model for Aerodynamic Flows.” 30th Aerospace Sciences Meeting and Exhibit, 1992.

[16] Morikuni, Keiichi, Lothar Reichel, and Ken Hayami. “Fgmres for Linear Discrete Ill-Posed Problems.” Applied Numerical Mathematics 75 (2014): 175–87.

[17] Toro, Elewterio F. “Flux Vector Splitting Methods.” Essay. In Riemann Solvers and Numerical Methods for Fluid Dynamics: A Practical Introduction, 249–50. Berlin: Springer, 1997.

[18] Roe, P.L. “Approximate Riemann Solvers, Parameter Vectors, and Difference Schemes.” Journal of Computational Physics 135, no. 2 (1997): 250–58.

[19] Yüksel, Ali Oğuz, and Yusuf Özyörük. “Navier-Stokes Computations of Helicopter Rotor Flow Fields,” 2017.

[20] Yıldırım, Berkay Yasin, and İsmail Hakkı Tuncer. “Aerodynamic Shape Optimization of a Wing Using 3D Flow Solutions with SU2 and Response Surface Methodology,” 2021.

[21] Bayliss, Alvin, and Eli Turkel. “Far Field Boundary Conditions for Compressible Flows.” Journal of Computational Physics 48, no. 2 (1982): 182–99.

[22] Flow of Fluids: Through Valves, Fittings, and Pipe. St-Laurent, Qué.: Crane Valves, 1987.

[23] Kandemir, Omer, and Fazil Selcuk Gomec. “Aerodynamic Nose Optimization of a Jet Trainer Aircraft.” AIAA AVIATION 2020 FORUM, 2020.

[24] Ansys. (n.d.). Ansys fluent users guide v19.2. Retrieved March 09, 2021.

[25] “Designs for Fitting the Second-Order Model.” Design and Analysis of Experiments, by Douglas C. Montgomery, 5th ed., 2001, pp. 456–462.

[26] Box, G. E., and K. B. Wilson. “On the Experimental Attainment of Optimum Conditions.” Journal of the Royal Statistical Society: Series B (Methodological) 13, no. 1 (1951): 1–38.

[27] Myers, Raymond H., Douglas C. Montgomery, and Christine M. Anderson-Cook. “Introduction.” Essay. In Response Surface Methodology: Process and Product Optimization Using Designed Experiments, 1–2. Hoboken: Wiley, 2016.

[28] Madamba, Ponciano S. “The Response Surface Methodology: An Application to Optimize Dehydration Operations of Selected Agricultural Crops.” LWT - Food Science and Technology 35, no. 7 (2002): 584–92.

[29] Mooij, E., K. Sudmeijer, and F. Kremer. “Aerodynamic Design of a Low-Cost Re-entry Test Vehicle Using a Taguchi Approach.” 9th International Space Planes and Hypersonic Systems and Technologies Conference, 1999.

[30] Carlson, Rolf, and Johan E. Carlson. “Summary of Screening Experiments.” Essay. In Design and Optimization in Organic Synthesis. Amsterdam: Elsevier, 2005.

[31] Lenth, Russell V. “Lenth's Method for the Analysis of Unreplicated Experiments.” Wiley StatsRef: Statistics Reference Online, 2014.

[32] Bühler, W. K. "The Method of Least Squares." Gauss, 1981, 138–41.

[33] Goldberg, David Edward. Genetic Algorithms in Search, Optimization, and Machine Learning. Addison-Wesley, 2012.

[34] Deb, K., et al. "A Fast and Elitist Multiobjective Genetic Algorithm: NSGA-II." IEEE Transactions on Evolutionary Computation, vol. 6, no. 2, 2002, pp. 182–197.

[35] Bao, Chunteng, Lihong Xu, Erik D. Goodman, and Leilei Cao. "A Novel Non-Dominated Sorting Algorithm for Evolutionary Multi-Objective Optimization." Journal of Computational Science. Elsevier, September 25, 2017.

[36] Roache, P. J. "Perspective: A Method for Uniform Reporting of Grid Refinement Studies." Journal of Fluids Engineering, vol. 116, no. 3, 1994, pp. 405–413.

APPENDICES

A. Non-dominated Sorting Genetic Algorithm-II Python Code

```
"""

Created on Sun Jan 10 21:43:17 2021

@author: omer

"""

import numpy as np

class Problem:

    def __init__(self, num_var, min_var, max_var):

        self.num_var = num_var # # of independent variables(genes)

        self.min_var = min_var # minimum constraint array for variables

        self.max_var = max_var # maximum constraint array for variables

class GaParameters:

    def __init__(self, max_it, pop_size, p_cross=1, gamma=0.01, p_mutation=0.01

             , beta=0.01, sigma=0.01):

        self.max_it = max_it # # of iterations for GA operations

        self.pop_size = pop_size # population size

        self.p_cross = p_cross # cross-over probability %/100

        self.num_cross = int(round(p_cross * pop_size / 2) * 2)

        self.gamma = gamma # cross-over step size

        self.p_mutation = p_mutation # mutation probability %/100
```

```
     self.beta = beta # primary mutation step size argument
     self.sigma = sigma # secondary mutation step size argument
class Population:
   def __init__(self, position, cost, subset, dom_count, rank , front, crowd_dist ):
     self.position = position # position of genes in design space
     self.cost = cost # cost value of genes
     self.subset = subset # individual list that ith individual dominates
     self.dom_count = dom_count # individual list that ith individual dominates
     self.rank = rank # rank of individuals
     self.crowd_dist = crowd_dist # crowding distance of genes
     self.front = front # front list of genes
   def __repr__(self):
     return "Population with position = " + str(
       self.position) + " , cost = " + str(self.cost)
   @classmethod
   def from_initial_population(cls, params, problem):
     # Select random individuals
     position = np.random.uniform(problem.min_var, problem.max_var,
                                  size=[params.pop_size, problem.num_var])
     # Evaluate cost for individuals
     cost = cost_function(position, problem)
     subset = sub_set(cost)
```

```
    dom_count = domination_count(cost)

    rank, front = rank_evaluation(subset, dom_count)

    crowd_dist = crowding_distance(rank, front, cost)

    return cls(position,  cost, subset,  dom_count, rank, front, crowd_dist)

@classmethod

def from_parent_selection(cls,pop,tournament_size = 3):

    # Select Parents

    parent_index = parent_selection(pop, tournament_size)

    position = pop.position[parent_index]

    cost = pop.cost[parent_index]

    rank = pop.rank[parent_index]

    subset = pop.subset[parent_index]

    front = []

    dom_count = pop.dom_count[parent_index]

    crowd_dist = pop.crowd_dist[parent_index]

    return cls(position,  cost, subset,  dom_count, rank, front, crowd_dist)

@classmethod

def from_crossover(cls,  parents, params, problem):

    offsprings = np.empty([params.num_cross / 2, problem.num_var, 2])

    for i in range(params.num_cross / 2):

        offsprings[i,  :, 0], offsprings[i,  :, 1] = crossover(parents,

                                              params)
```

```
    position = offsprings.reshape([params.num_cross, problem.num_var])

    position = np.maximum(position,problem.min_var)

    position = np.minimum(position,problem.max_var)

    cost = cost_function(position, problem)

    subset = sub_set(cost)

    dom_count = domination_count(cost)

    rank, front = rank_evaluation(subset, dom_count)

    crowd_dist = crowding_distance(rank, front, cost)

    return cls(position, cost, subset, dom_count, rank, front, crowd_dist)

@classmethod

def from_sorting(cls, pop, popc, params):

    # Merge Parents and Offsprings

    position = np.vstack((pop.position, popc.position))

    cost = np.vstack((pop.cost, popc.cost))

    subset = sub_set(cost)

    dom_count = domination_count(cost)

    rank, front = rank_evaluation(subset, dom_count)

    crowd_dist = crowding_distance(rank, front, cost)

    so_list = np.vstack([rank, crowd_dist]).transpose()

    so = np.lexsort((-so_list[:,1], so_list[:,0]))

    position = position[so[0:params.pop_size], :]

    cost = cost[so[0:params.pop_size], :]
```

```
        subset = sub_set(cost)

        dom_count = dom_count[so[0:params.pop_size]]

        rank, front = rank_evaluation(subset, dom_count)

        crowd_dist = crowd_dist[so[0:params.pop_size]]

        return cls(position,  cost, subset,  dom_count, rank, front, crowd_dist)

. . . Shortened version . . .
```